A-Site Deficient Lanthanum Strontium Chromite Oxide with In-Situ Growth of Ni-

Co Nano-Alloys: A Potential Electrode Catalyst for Solid Oxide Fuel Cell

by

Lin Cui

A thesis submitted in partial fulfillment of the requirements for the degree of

Master of Science

In

Chemical Engineering

Department of Chemical and Materials Engineering

University of Alberta

ABSTRACT

Solid oxide fuel cell (SOFC) is an advanced power generation device that has desirable fuel flexibility and higher efficiency compared to conventional electricity generators. Since SOFC requires different fuel gases for reactions, a catalytically active fuel electrode with excellent stability as well as good carbon deposition resistance is the real challenge for the cell. In this research, the in-situ exsolved bimetallic doped A-site deficient perovskite oxide: A-site deficient nickel (Ni) and cobalt (Co) bimetallic doped lanthanum strontium chromite oxide (LSC) has been fabricated as a potential fuel electrode for SOFC. The in-situ exsolution process of Ni-Co alloy has been elaborately studied from various aspects. The electrochemical performances of Ni-Co doped LSC are thoroughly compared with Ni doped LSC in hydrogen gas, syngas as the anode and in CO_2 gas as the cathode. The fuel cell with a bimetallic doped LSC anode has shown maximum power densities of 329 mW/cm^2 in hydrogen and 258 mW/cm^2 in syngas compared with only 237mW/cm^2 in hydrogen and 170 mW/cm^2 in syngas for the fuel cell with the single metallic doped anode at 850°C. The Ni-Co doped electrode also has shown higher optimum operating voltage and better stability than the Ni doped electrode in cathode function. Ni-Co doped cells have demonstrated no obvious degradation during long-term operation as well as good carbon deposition resistance under the tested atmosphere. It can be postulated that the existence of A-site deficiency helps the formation of oxygen vacancies as well as enhances the

reducibility of B-site ions. Meanwhile, the synergistic effect between Co and Ni has changed the reduction behavior of Ni particles that increased its reducibility and promoted its electrochemical performances as well as the carbon deposition resistance.

Acknowledgement

I would like to give my most sincere appreciation to my dear supervisor, Dr. Jingli Luo for all the guidance and encouragement from her. It was her great patience and understandings that encouraged and pacified me when I struggled with problems and troubles. The knowledge and ideas I have received from her not only helped me to accomplish my research in past two years, but also opened up my eyes to a wider vision of the world. I am so proud to be one of her students.

I am also grateful to Dr. Yifei Sun, Yaqian Zhang and Dr. Bin Hua for all of their valuable advice and suggestions that guided me throughout my whole research process and thesis writing period. Their knowledge and supports make my study life here extremely fun and unforgettable.

I also wish to thank my colleagues and friends, Xianzong Wang, Subiao Liu, Wenfei Wang, Shuo Shuang, Jiankuan Li, Minkang Liu, Ermia Aghaie, and Dr. Yashar Behnamianfor all their support and encouragement during my study life in this group.

In the end, I wish thank my parents for their love and support. Their unconditional trust and love provide me the endless courage to pursue my dream and face the challenges in the future.

Table of Contents

List of Figures

List of Tables

List of Symbols

A	Pre-Exponential Factor
d	Distance Between the Atomic Layers of Crystal
E	Reversible Voltage
E^0	Standard Reversible Voltage
E_a	Activation Energy
E_ω	Frequency Dependent Potential
F	Faraday Constant
ΔG	Change in Gibbs Free Energy
I_ω	Frequency Dependent Current
j	Current Density
k	Rate Constant
λ	Wavelength
n	Mole of electrons transferring during the reaction
n	Integer
η_{act}	Activation Polarization
η_{conc}	Concentration Polarization
η_{ohmic}	Ohmic Polarization
P	Produced power density
p	Partial pressure
r_A	Ionic Radius of Atom A
r_B	Ionic Radius of Atom B
r_o	Ionic Radius of Oxygen
R	Universal Gas Constant
θ	Angle of incidence

T	Temperature
t	Tolerance Factor
δ	Oxygen Vacancies
V	Voltage output
W	Electrical Work
Z_ω	Frequency Dependent Resistance (Impedance)

List of Abbreviations

AE	Alkaline Earth
AFC	Alkaline Fuel Cell
BE	Backscattered Electrons
EDS	Energy Dispersive X-ray Spectroscopy
EDTA	Ethylene Diamine Tetra Acetic Acid
EIA	International Energy Agency
EIS	Electrochemical Impedance Spectroscopy
GC	Gas Chromatography
GDC/ CGO	Gadolinium-Doped Ceria
GHG	Greenhouse Gas
LCC	$LaCaCrO_{3-\delta}$
LSC	Lanthanum Strontium Chromite Oxide
LSC	$LaSrCrO_{3-\delta}$
LSCF	Strontium and Cobalt Doped Lanthanum Ferrite Oxide
LSM	Strontium-Doped Lanthanum Manganite Oxide
MCFC	Molten Carbonate Fuel Cells
MS	Mass Spectrometry
MTOE	Million Tons of Oil Equivalent
OCV	Open Circuit Voltage
PAFC	Phosphoric Acid Fuel Cells
PEM	Polymer Electrolyte Membrane
SE	Secondary Electrons
SEM	Scanning Electron Microscopy
SOEC	Solid Oxide Electrolysis Cell

SOFC	Solid Oxide Fuel Cell
TGA	Thermogravimetric Analysis
TPB	Triple Phase Boundary
TPO	Temperature Program Oxidation
TPR	Temperature Programmed Reduction
TWh	Terawatt Hours
XRD	X-Ray Diffraction
YSZ	Yttria Stabilized Zirconia

Chapter 1 Background Information

The Fossil Resource Consumption

The rapid growth of the world's energy consumption in recent years, and subsequent increase in GHG (greenhouse gas) emissions, has raised serious concerns about heavy environmental impacts such as global warming and climate change.[1] Figure 1.1 a) and b) depict the fuel consumption and fuel electricity generation trends of the last four decades, respectively. These data have been collected and revealed by the International Energy Agency (EIA) 2015. From 1973 to 2013, the world total final consumption of fuel has grown by 99.3% (4667 Mtoe (Million Tons of Oil Equivalent) to 9301 Mtoe). As the second largest energy resource in the world, the consumption proportion of the electricity is almost doubled in last four decades (from 9.4% to 18.0%). In terms of electricity generation, fossil fuels still play a significant role as depicted in Figure 1.1(b) that most of the electricity is generated by fossil thermal method, and the amount of generated electricity has increased by 280% (6131TWh to 23322 TWh).[2]
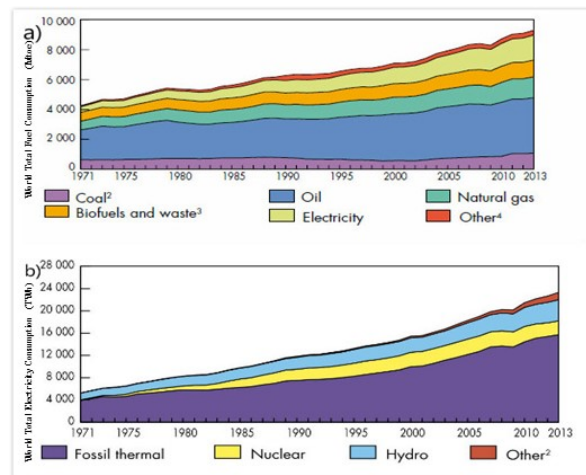
Figure 1.1. a) The world final consumption by fuel from 1971 to 2013. b) The world electricity generation from 1971 to 2013.[2]

To mitigate the massive usage of fossil fuels for electricity generation, efforts can be placed onto the investigation of novel energy generation methods with higher conversion efficiency with environmentally friendly, low pollution conversion emissions, such as the electrochemical approach.

1.2 Fossil Thermal Power Generation, Fuel Cells and SOFC

1.2.1 Fossil Fuel Power Generation

As illustrated in Figure 1.2, a traditional thermal power station contains a complicated energy conversion process. At first, the chemical energy contained in fossil fuels is converted into thermal energy through combustion. The thermal energy is then applied to a steam boiler to generate mechanical energy with the use of a steam turbine, and at last, electricity is produced by transforming mechanical energy using a generator.[3] Throughout the process of converting chemical energy into electricity, a loss of energy can be expected at each of the four conversion steps. In addition, on-site water processing and pollution control facilities also consume a part of the produced electricity. As a result, modern steam cycling thermal power stations have an efficiency of only around 40%.[4] Therefore, from the overall point of view, the operation of a fossil thermal power station contains unavoidable limitations that constrain its development for higher energy conversion efficiency.
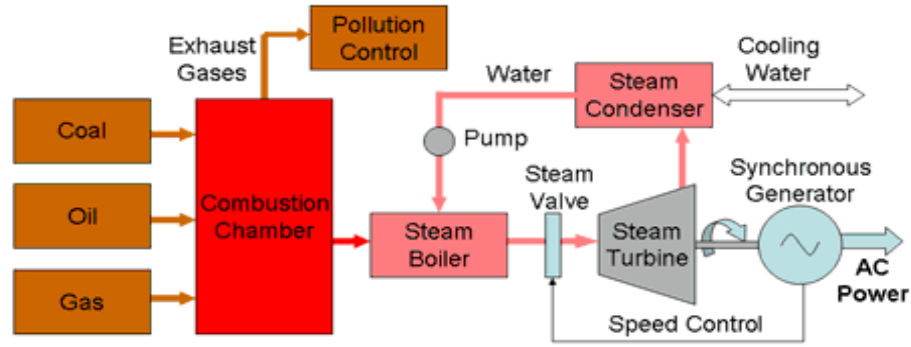
Figure 1.2. The schematic diagram of traditional thermal power station.[3]

In contrast to the lengthy and inefficient four step conversion process used in power stations, fuel cell research has depicted a more direct pathway, one with a simpler operating process to convert chemical energy into electricity with emissions of only water or with small amount of nearly pure CO_2.[5] Fuel cell technology provides great potential in the area of high-efficiency fossil fuel conversion. Therefore, compared to the traditional fossil fuel thermal power generation process, the use of fuel cells and electrochemical processes provide a cleaner energy producing technology which focuses on the improvement of energy generation efficiency and fossil fuel consumption reduction.[6]

1.2.2. Fuel Cells and SOFC

A fuel cell is a device that uses electrochemical processes to directly convert chemical energy into electricity. This process is also done in a manner that provides significant environmental advantages with regard to the low pollutant and GHG emission aspects. [6,7] Nowadays, different types of fuel cells are developed based on the same operating principle as shown in Figure 1.3. In a fuel cell system, the fuel electrode (anode) contains a porous electrode where the oxidation of the fuel gas occurred. Oxygen (from the air) comes into contact with the air electrode (cathode), which undergoes reduction processes to form oxide ions. Protons or oxide ions are transported through the electronically insulating electrolyte.

Water is produced as the final product of the reaction and electricity is generated by the flow of electrons that is delivered to the external circuit.[7] The reaction equations are listed as equations 1 and 2.
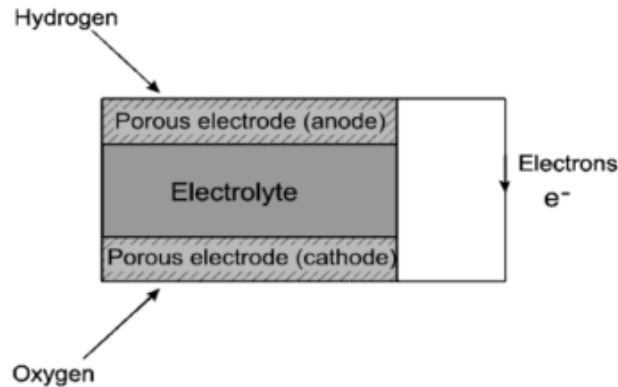
Figure 1.3. The schematic diagram of the fuel cell operating principle.[7]

$$H_2 + O^{2-} \rightarrow H_2O + 2e^- \quad (1) \, (\text{Anode})$$
$$O_2 + 4e^- \rightarrow 2O^{2-} \quad (2) \, (\text{Cathode})$$
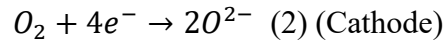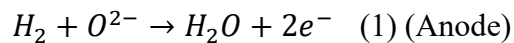
The five main types of fuel cell are shown in Table 1.1. These fuel cells are classified based on the different types of materials used for the ionic conductors, the electrolyte.[6] The alkaline fuel cell (AFC) conducts OH⁻ ions from the cathode to the anode using a strong alkaline solution (sodium/potassium hydroxide Na/KOH) as the electrolyte. AFC's, the oldest type of fuel cell technology, require very pure hydrogen as the fuel source and air/pure oxygen as the oxidant. Phosphoric acid fuel cells (PAFC) use a concentrated phosphoric solution to conduct H⁺ with hydrogen or syngas as the fuel. Polymer electrolyte membrane (PEM) fuel cells, also known as the proton exchange fuel cells and solid polymer fuel cells are operating based on the proton conducting membrane electrolyte to transfer H⁺ from anode to cathode. In this case, only pure hydrogen is considered as the proper fuel source. In the case of molten carbonate fuel cells (MCFC), a molten potassium

lithium carbonate electrolyte is applied to conduct CO_3^{2-} from the cathode to the anode. Syngas is considered to be a suitable fuel for MCFC. Finally, the SOFC utilizes hydrogen from hydrocarbons at the anode and oxygen from air at the cathode to produce electricity. SOFC has the highest operating temperature compared to other fuel cells as ceramics are selected as the electrolyte. Both the ion and proton conductor electrolytes are investigated for SOFC.[7]

Table 1.1. Five main types of fuel cell. [7]

Fuel Cell	Electrolyte	Operating Temperature (ºC)
Alkaline (AFC)	Sodium/ Potassium Hydroxide	70
Phosphoric Acid (PAFC)	Phosphoric Acid	200
Polymer Electrolyte Membrane(PEM)	Polymer Membrane	80
Molten Carbonate (MCFC)	Molten Salt	650
Solid Oxide (SOFC)	Ceramic	750-1000

The SOFC has been considered the most efficient power generating fuel cell with an efficiency of up to 70% and an additional 20% which can be recovered from heat. Unlike other fuel cells, SOFC has the most flexible choice of fuels and can generate electricity from many carbon-based fuels such as syngas and natural gas.[6] Moreover, the high temperature operating conditions of SOFC provide a suitable environment for the internal anode reforming process to take place, Additionally, the high temperatures also allow for rapid electrocatalysis of hydrocarbon oxidation with the use of non-precious metals, which has effectively increased the overall electrical efficiency of the system.[8] Therefore, the SOFC in the study can be a potential solution for the current low efficiency fossil thermal

power generation system. In addition, companies like Bloom Energy in the U.S., California, has already investigated the applications, such as the Bloom's Energy Server® to bring the fuel cell technology into real life. The Bloom's Energy Server® is a new class of power generator based on SOFC technology that can generate about 200kW of power per unit server "in roughly the footprint of a standard parking space." [9]

Unfortunately, the current technology for SOFC is still not mature enough for large scale applications. Limitations are mainly caused by the complex fabrication processes for electrode materials, reduced cell lifetime due to the high operating temperature and the use of expensive ceramics and metals for the cell.[6] More investigations are still need to be done based on these challenges for the industrialization process of SOFC in the future.

1.3 Thesis Objectives and Contents

The objective of this thesis is to (a) investigate a promising electrode material that has excellent stability under various fuel gas atmosphere at a high operating temperature and good electrochemical catalytic activity for the conversion process of SOFC, (b) to understand the cell performance and the mechanism of degradation of the cell during operation.

Chapter 2 describes the main principles behind the performance of SOFC and summarizes the proper anode materials based on the different properties required from the operating principle. The experiment methodology, including the synthesis of materials, the detailed experimental procedure, fuel cell set-up, electrochemical tests and characterization methods are described in Chapter 3. Chapter 4 is mainly focused on the characterization results and electrochemical performance and discussion. Conclusions and future work are presented in Chapter 5.

Chapter 2 Literature Review

2.1 Thermodynamics of SOFC

The electrochemical reaction that occurs in SOFC can be represented through the fundamental rules of thermodynamics in terms of power output and maximum voltage. The maximum electrical work (W) can be performed by the negative value of the change in Gibbs free energy (ΔG):

$$W = -\Delta G \ (3)$$

where the reversible voltage can be shown as:

$$E = \frac{W}{nF} = \frac{-\Delta G}{nF} \ (4)$$

where E is the reversible voltage, n is the mole of electrons transferring during the reaction, and F is Faraday's constant.

The SOFC reaction with H_2 gas as fuel is:

$$\frac{1}{2}O_2 + H_2 = H_2O \ (5)$$
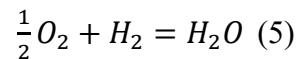
The reversible voltage can be calculated by Nernst Equation:

$$E = \frac{-\Delta G}{2F} = E^0 - \frac{RT}{2F} \ln \frac{p_{H_2O}}{p_{H_2} \ (p_{O_2})^{\frac{1}{2}}} \ (6)$$

where E^0 is the standard reversible voltage, R is the universal gas constant, p_{H2O}, p_{H2}, and p_{O2} are the partial pressures of the steam, hydrogen and oxygen, respectively.

2.2 Cells Performance and Polarizations

The performance of an SOFC is often described by its voltage-current (j-V) relationship, as shown in Fig. 2.1.[10] Compared to the ideal thermodynamic cell voltage the real voltage

produced by SOFC is decreased substantially by several unavoidable losses. The measured open circuit voltage (OCV) of the cell is lower than the theoretical reversible voltage due to the internal electrical short circuiting from the small electronic conductivity of the electrolyte, and the leakage of fuel gases. Activation polarization (η_{act}) occurs at lower current density range that is mainly due to the loss in the electrochemical reaction. Ohmic loss (η_{ohmic}) determines the performance at the midrange current density region which depends on the ionic and electronic conductivity of the cell. In addition, in the high current region, concentration polarization (η_{conc}) dominates and leads to a precipitous drop of the voltage for SOFC.
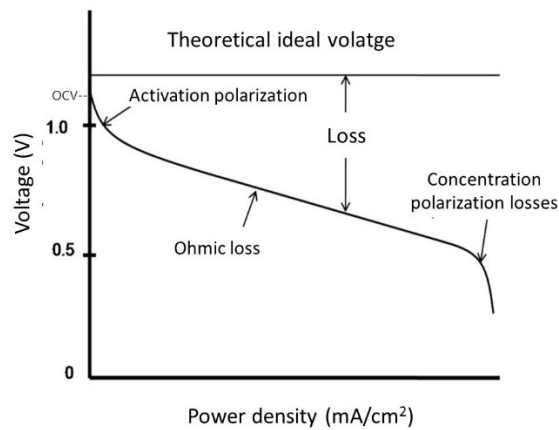
Figure 2.1. Typical j-V performance of a SOFC. [10]

Therefore, the real voltage produced by the SOFC can be expressed as equation (7) as shown below. These losses reduce the SOFC energy utilization rate in the cell reaction process. Thus, to improve the cell performance, it is critical to reduce the resistance of the cell, and accelerate the electrochemical reaction rate and mass transport rate of reactants and products. Therefore, it is necessary to study the ionic and electronic conductivity, electrochemical catalytic activity and porosity of the cell material.

$$V = OCV - \eta_{act} - \eta_{ohmic} - \eta_{conc} \quad (7)$$

2.3 Triple Phase Boundary

Due to the fact that the reactions for SOFC involve ions, electrons and the gas phase molecules that come from three different phases, the interphases of the electrode material and the electrolyte material with the gas phase play a significant role in the overall cell performance, which is described as the triple phase boundary (TPB).[11]

Figure 2.2 shows a simple schematic diagram for the TPBs. As shown in the diagram, the existence of TPBs provides the pathways for the ions, electrons and gas molecules to meet and react, the electrochemical reaction will only occur at the TPBs. Thus, the TPBs are also named as the 'active sites' or 'reaction sites'. As the result, with the important implications of the TPBs, a highly porous nano-structured electrode material is always demanded for the gaseous diffusion purpose and the intimate contact between the gas, electrode, and the electrolyte.
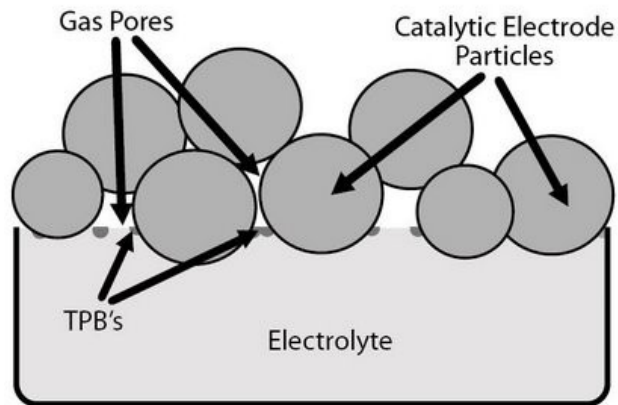
Figure 2.2. The schematic diagram for triple phase boundaries.[12]

2.4 Electrolyte Materials

Oxygen ion conductive electrolyte is considered as the preferable material for this research. The electrolyte layer has multi functions in an SOFC. The main requirements for the electrolyte are to separate the fuel gas and air from the fuel electrode and the oxygen electrode, respectively, as well as to provide enough ionic conductivity for the oxygen ion conducting electrolyte while preventing the conduction of the electrons from electrodes.

Over last two decades, the yttria stabilized zirconia (YSZ) electrolyte has been mainly developed for the high temperature fuel cell operations, which has turned the material YSZ into one of the most popular candidates for SOFC electrolytes. Previous studies on YSZ has shown its extraordinary ionic conductivity and negligible electronic conductivity with superb stability under both of the oxidizing and reducing environments.[13,14] These properties of YSZ make it exactly the electrolyte material people are looking for in an SOFC. Thus, YSZ is also selected as the electrolyte material for this research.

Besides YSZ, other materials like ceria (CeO_2) based materials are receiving more attention recently due to their higher ionic conductivity than YSZ. However, these kinds of materials are prone to have the electronic conductivity at the low oxygen partial pressure atmosphere, especially in the reducing fuel environment. Hence, this limitation constrains their development in practical SOFCs.[14,15]

2.5 The Oxygen Electrode Materials

The oxygen electrode is the place where the oxygen reduction in SOFC happens. Air is often fed to the oxygen electrode and oxygen in the air reacts on the electrode; hence oxygen electrode is also as known as the air electrode. For SOFC, oxygen diffuses through

the porous cathode electrode to the TPB that gets driven through a reduction reaction to become oxygen ions that transport through the electrolyte to the anode side. A satisfactory oxygen electrode material is expected to have high catalytic activity, sufficient electronic and ionic conductivities, excellent porosity for gas diffusion to the TPBs, and good stabilities to withstand the high operating temperature and the high oxygen partial pressure.

Noble metal catalysts have been considered as suitable air electrode materials due to their high conductivities, especially platinum, Pt. However, due to the high cost of noble metals, Pt is not considered as a potential candidate for oxygen electrode in this research. Metal oxides with good conductivities are concerned as alternatives to Pt for the air electrode.[16]

Perovskite-based materials have been found as the most adaptive choice for applications related to oxygen evolution reactions. The strontium-doped lanthanum manganite oxide (LSM) is a typical oxygen electrode material as a composite of LSM/YSZ. This composite provides reasonable catalytic activity as well as good stability and conductivity under different oxygen partial pressures.[17] Recently, strontium doped lanthanum ferrite oxide with partial substitution of cobalt (LSCF) has been proposed as an alternative oxygen electrode for SOFC. It has demonstrated much improved electrochemical catalytic activity than the composite of LSM/YSZ.[18] Due to the poor compatibility between the LSCF and YSZ, a barrier layer of gadolinium-doped ceria (GDC, also known as CGO) is often applied between the LSCF-YSZ interfaces to prevent further side reactions. Even though the interlayer sintered between the GDC and YSZ electrolyte shows a lower ionic conductivity than YSZ itself [19], investigations still have stated that the composite of LSCF-GDC is electrochemically more stable than LSM-YSZ with higher performances.[20] Therefore, in this research, the LSCF-GDC composite is selected to be the oxygen electrode.

2.6 Fuel Electrode Materials

The fuel electrode plays an important role in SOFC applications since the electrochemical oxidation of the fuel gas processes occur at the anode side of the SOFC. The reaction rates of the fuel gas are considered as the rate-determining steps for SOFC that can directly affect the overall conversion efficiency of the cells. Thus, fuel electrodes are usually required to have high catalytic activities, good conductivities, good porosity for gas diffusion processes, and chemical and mechanical compatibilities with electrolytes and interconnectors. Moreover, the fuel electrode usually gets directly contacted with various fuel gases that have different characteristics. Therefore, excellent chemical and mechanical stabilities under different fuel gas atmospheres and redox treatments are especially essential for the selection of fuel electrode materials.

2.6.1 Ni-YSZ and Existing Limitations

The noble metal Pt has been proven as a good electrode material with high conductivities, however, the transition metal, Ni has an even better performance than Pt as a fuel electrode material over 700°C.[20] Thus, a conventional design of composite Ni-YSZ cermet has been most investigated for the use of the SOFC fuel electrode. This composition provides excellent ionic conductivity through YSZ and sensational electronic conductivity and catalytic activity by Ni particles.[21] As the Ni-YSZ gets tested under increasing amount of applications with various conditions, some severe limitations and problems for the Ni-YSZ composite have occurred .

a. The Ni-YSZ has a strong tendency to promote carbon deposition under the fuel gas environment of syngas (CO&H_2) and hydrocarbons for SOFC (can be detected by SEM).[22] As expressed in Figure 2.3, Ni and YSZ particles with a size of 1 to 2 μm have formed large amount of cokes within their structure after only 4 hours of

operation at 600°C that have blocked lots of apparent TPBs and degraded the overall performance. As well, the formed cokes even get dissolved into Ni particles and eventually destroy the Ni-YSZ structure at over 800°C.[22]
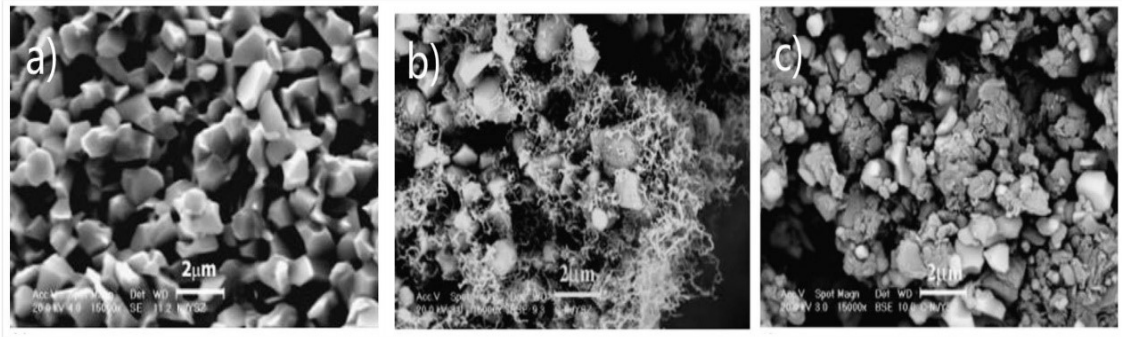
Figure 2.3. the SEM image of fresh Ni-YSZ a) Ni-YSZ after carbon deposition in methane (CH4) for 4 hour at 600◦C (873K) b) and 800◦C (1073K) c). [22]

b. For the reason of carbon deposition and oxidation of the catalytically active particle Ni, redox treatment for fuel electrode recovery is necessary for long-lasting operation. During the redox process, the deposited carbon can be oxidized into CO_2 and the NiO will be reduced as Ni to be recovered. Nevertheless, the Ni-YSZ composite possesses an inferior stability under redox cycling; the phase change of large size of Ni particles (1 to 2 μm) leads to a significant volume change of the microstructure during the redox process, from Ni to NiO to Ni, that will destroy the microstructure and eventually the cell.[23]

2.6.2 Perovskite Oxide Based Material

An alternative candidate for the fuel electrode for an SOFC is perovskite oxide. The perovskite oxide has an excellent thermal and mechanical stability under high temperature operating conditions, as well as good compatibility with the electrolyte material YSZ. Such

unique properties of the perovskite oxide bring it more possibilities for electrochemical applications.[24]

Perovskite oxide is the metal oxide with a cubic lattice structure of ABO_3 (Figure 2.4) that encompasses a variety of different components with very different properties.[25] Generally speaking, the A sites are occupied by the large (lower valent) cations: alkali, alkaline earth or rare earth metals with 12-coordination number in the periodic table, such as La, Sr, Ca and Pt, while the small cations at B sites come from transition metal ions with higher valent with 6-coordination numbers, such as Ti, Ni, Fe and Co.[25,24] As indicated in Figure 2.4[26] a), the B atom is at the center of an octahedral lattice formed by 6 oxygen atoms surrounding it and connected to one another; meanwhile each A atom is arranged at the site with 8 octahedra surrounding it (Figure 2.4 b). The relation between the radii of A, B and O^{2-} for the ideal cubic structure is shown as equation 8, where r_A, r_B and r_O are the radii of A,B and O^{2-} respectively.[24]

$$r_A + r_o = \sqrt{2}\ (r_B + r_o)\ (8)$$
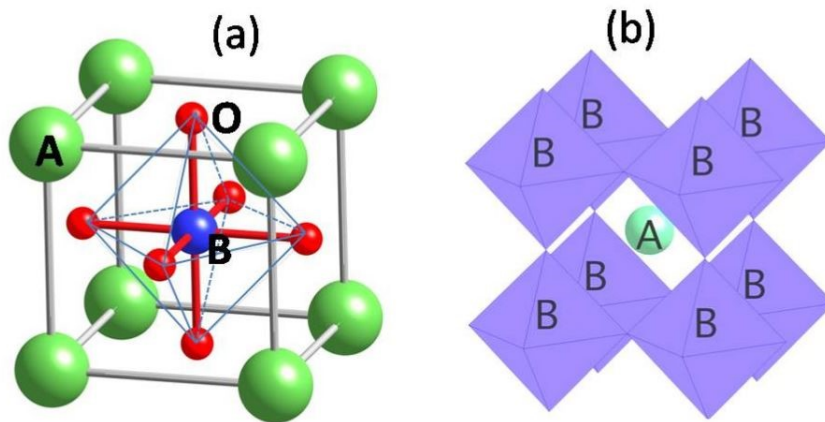
Figure 2.4. Crystal structure of perovskite oxide centered at a) B site atom, b) A site atom.[26]

Due to the complexity of perovskite oxides that various cations can be substituted at the sites, various levels of distortion of the structure can be expected. The Goldschmidt's tolerance factor describes the stability and distortion of the crystal structure as expressed by equation 9. The t value equals 1 when the perovskite is in the ideal cubic structure, and as t decreases, the unit lattice is shifting into triclinic by increasing distortion and losing stability. A stable structure of perovskite oxide is expected to have a t value between 1 and 0.89.[24] Based on the different properties revealed by different combinations of A&B site atoms, perovskite oxides can be widely applied on different areas of SOFC. The typical applications of perovskite oxides are listed in Table 2.1.[24]

$$t = \frac{r_A + r_o}{\sqrt{2}(r_B + r_o)} \quad (9)$$

Table 2.1. Typical perovskite oxide applications for solid oxide cells.[24]

Component	Perovskite Oxide
Oxide Electrode	$La(Sr)MnO_{3-\delta}$, $La(Sr)CoO_{3-\delta}$, $Sm_{0.5}Sr_{0.5}CoO_{3-\delta}$, $La(Sr)Fe(Co)O_{3-\delta}$
Electrolyte	$La(Sr)Ga(Mg)O_{3-\delta}$ (O^{2-}), $BaCeO_{3-\delta}$ (H^+), $BaZrO_{3-\delta}$ (H^+), $SrZrO_{3-\delta}$ (H^+)
Fuel electrode	$La_{1-x}Sr_xCr_{1-y}M_yO_{3-\delta}$ (M= Fe, Co, Ni), $SrTiO_{3-\delta}$
Interconnector	$La(Ca)CrO_{3-\delta}$

2.6.2.1 Lanthanum Chromite Perovskite Oxide

The pure lanthanum chromite perovskite oxide, $LaCrO_{3-\delta}$, is a p-type pure electron conductor with low electronic conductivity. However, $LaCrO_{3-\delta}$ has a tolerance factor of 0.97, which results in superb chemical, mechanical and thermodynamic stability.[24, 27] By doping alkaline earth (AE) elements at A site, $La_{1-x}M_xCrO_{3-\delta}$ (M=Ca, Sr) becomes a good electronic conductor with enhanced ionic conductivity, which is often used as the interconnect of the SOFC (Table 2.1). Doping of the bivalent element Sr or Ca at the A site not only leads to Cr^{3+} to Cr^{4+} transition that creates more electronic holes in the valence band and thus improves the electronic conductivity, but also creates oxygen vacancies that give rise to ionic conductivity by charge compensation.[28] In addition, since the Cr^{3+} ion has strong capability to maintain a six-fold oxygen ion coordination under both oxidizing or reducing atmospheres, the electronic conductivity of the perovskite is maintained as much as possible under low oxygen partial pressure condition.[29,30]

Moreover, Ca, Sr doped $LaCrO_{3-\delta}$ has a great potential to be a fuel/oxygen electrode as well. Since $LaCrO_{3-\delta}$ has well-known good stability during high temperature operation, the stabilities of $LaSrCrO_{3-\delta}$ (LSC) and $LaCaCrO_{3-\delta}$ (LCC) under oxidizing and reducing environments were tested by Sfeir.[31] This study illustrates that under the oxidizing condition, the Ca doped $LaCrO_{3-\delta}$, becomes much more stable than the Sr doped one, whereas in a reducing atmosphere, Sr doped $LaCrO_{3-\delta}$ successfully preserved the perovskite phase while Ca has highly destabilized the structure.[31]

2.6.2.2 Wet Impregnation and In-situ Exsolution

LSC is a potential fuel electrode material with good stability, mechanical properties and conductivities, but it suffers from the problem of low catalytic activity. To solve this

problem, people are considering introducing other catalytically active metal nanoparticles like Ni or Co to incorporate them with the existing structure of LSC by wet impregnation (infiltration) or chemical deposition.

The wet impregnation method is a well-known technique for the preparation of heterogeneous catalysts as well as applications to enhance anode/cathode performance for SOFC.[32] By infiltrating metallic catalyst solutions into the sintered porous perovskite-based skeleton, uniformly distributed metallic nanoparticles are expected to establish in the electrode and lead to the improvements in TPBs, electronic conductivity and catalytic activities as demonstrated in Figure 2.5.[33] However, the agglomeration phenomena of the nanoparticles have occurred during the long-term repeated sintering process after infiltration that has dramatically increased the particle sizes and its tendency for carbon deposition. Therefore, particle agglomeration has consequently decreased the amount of TPBs as well as the uniformity of the distribution and thus the cell stability and its overall performance.
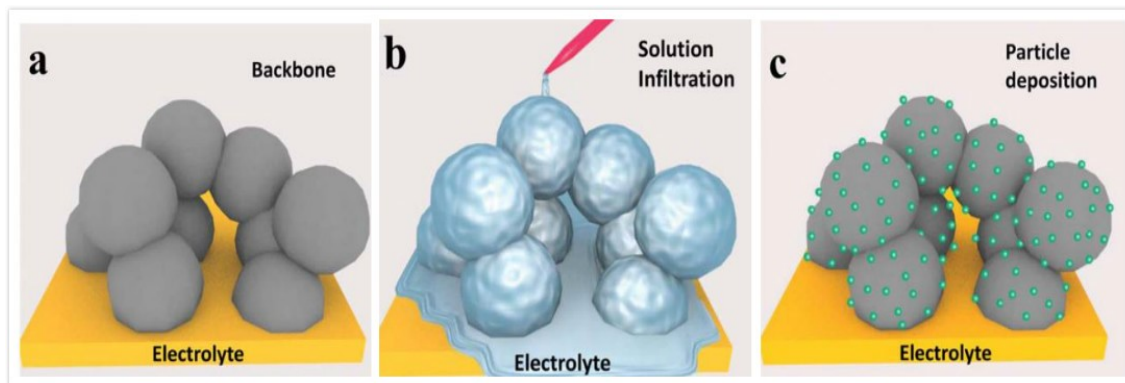
Figure 2.5. Schematic of typical wet infiltration method.[33]

Alternatively, the in-situ exsolution method has been investigated for this situation to achieve smaller sized, highly uniformly distributed nanoparticles on the electrode material with elevated carbon deposition resistance and improved electrochemical performance.[34,35] In-situ means at the original position. The main idea of in situ exsolution is to dissolve catalytic transition metals inside the perovskite structure (at B sites) and make it partially exsolve out of the lattice in a reducing atmosphere in order to form a highly uniform dispersed decoration of nanoparticles on the perovskite support. By comparing with the infiltration method in Figure 2.6, the unavoidably long cycling sintering process for impregnation is continuously promoting the agglomeration of nanoparticles, while in-situ exsolution can prevent it by only requiring one high temperature sintering for material fabrication from the original. Therefore, the agglomeration phenomena can be successfully reduced by the in-situ exsolution process. [28,36]
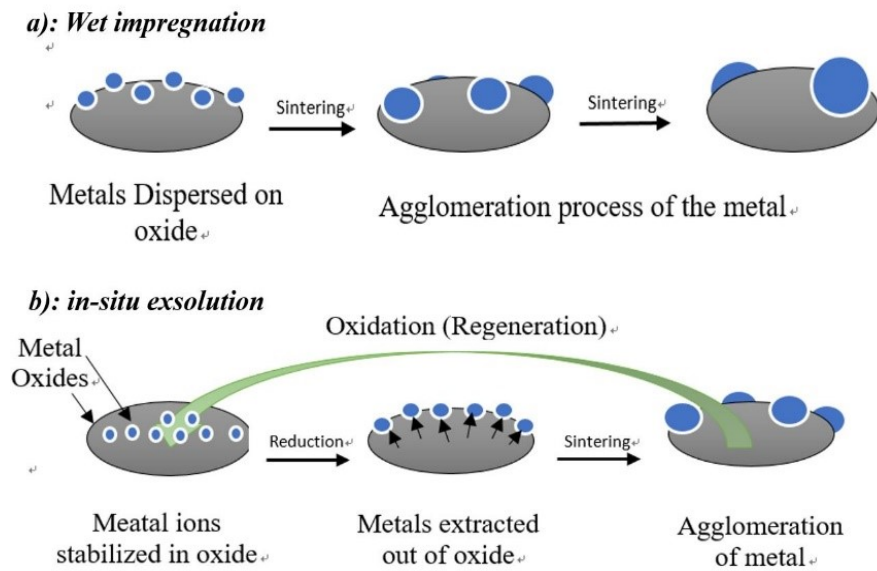
Figure 2.6. Schematic of a) wet impregnation process, b) in-situ exsolution.

In-situ exsolution suggests an extraordinary pathway for catalytic particles of Ni, Co or Fe to partially substitute into the B-site of the LSC lattice to turn LSC into a potential anode material (fuel electrode) for SOFC as listed in Table 2.1. Doping of transition metals into B sites of LSC imparts both electron holes and oxygen vacancies into the structure as well as brings their high electronic conductivity, catalytic activity and a large amount of TPBs to the support material. Moreover, the in-situ doped nanoparticles even have demonstrated a fabulous carbon deposition resistance as well as thermal and redox stability compared with chemical infiltration during high temperature operation.[37] The lattice structure for chemical infiltration and in-situ exsolution is shown in Figure 2.7 that illustrates the exsolved particles are acting pinned into the lattice at its original position which expresses a promoting stability at the metal particle/oxide support interface instead of simply depositing the catalytic metals onto the bulk oxide. In the meantime, the morphological differences also affect the growing mechanism of carbon fibers by carbon deposition appearance as shown in Figure 2.8. Based on the study of Neagu et al[38], the carbon fiber growth on Ni particles is following the "tip growth" mechanism for deposited nanoparticles, that carbons get dissolved into the Ni lattice at first, then grow up at the metal/oxide interfaces to uplift the Ni particles from the in original places; thus it can destroy the structure and deactivate the cell. Nevertheless, due to the strong interactions between the exsolved "socketed" Ni particles and parent oxide support, the particle uplifting and subsequent carbon fiber growth are prevented. As the result, carbon fibers grow in a "base growth" mechanism that allows Ni particles to stay attached to the substrate while carbon fibers grow on top of it with considerably shorter length. Therefore, the in-situ exsolved particles are expected to maintain higher redox stability and better carbon deposition resistance during operation.
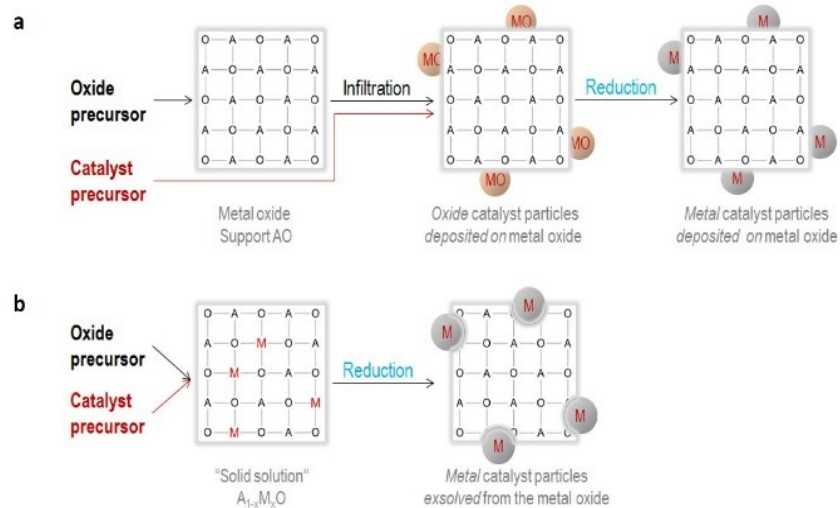
Figure 2.7. Decoration catalyst particles M through a) chemical infiltration b) in situ redox exsolution.[38]
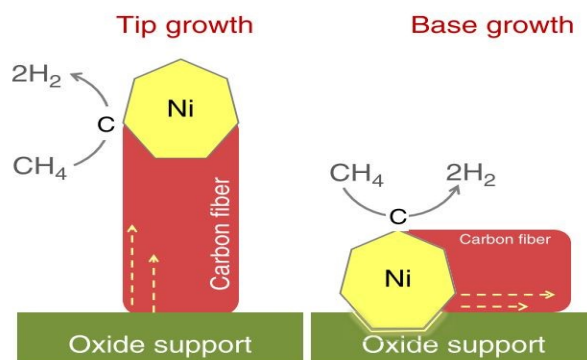
Figure 2.8. Schematic of possible carbon fiber growth mechanisms.[38]

2.7 Bimetallic Nanoparticles Doping and Perovskite Non-stoichiometry

In order to further improve the performance of doped LSC perovskite, bimetallic doping and perovskite non-stoichiometry, two aspects are concerned to boost carbon deposition resistance, in situ exsolution appearance and catalytic activity.

Bimetallic doping is the idea to introduce a second metal (guest metal) to the host metal as a promoter to optimize the monometallic property. Metal alloys, especially Ni-alloys, were tested to have sufficient effects on the mitigation of inducing carbon into the structure that successfully suppressed formation of carbon fibers.[39] High catalytic Ni is selected as the host metal for the LSC support, and Co is concerned as the proper guest metal due to its good electrochemical activity and high tolerance of coking.[40] Grgicak et al.[41] have studied the comparison of Ni-Co alloy compared to single Ni metal; the result shows that Ni-Co alloy can successfully decrease the exsolved particle sizes and increase the total surface area and TPBs. Ni-Co alloy expresses highly stable activity and promotes electrochemical activity under carbon containing environment over a wide range of temperature ($500°C$ to $900°C$), which suggests the combination of Ni and Co can indeed prevent the deactivation phenomena by carbon deposition. [40,41] Different ratios of Ni/Co were tested by Takanabe et al.[40] from 0:100 to 100:0, and the results demonstrate that the catalytic activity gradually increases with increased Ni content, while the coke resistance rises with the amount of Co content. Therefore, a proper ratio of Ni and Co needs to be considered for the tradeoff between reaction activity and coking resistance.

Most of the in-situ exsolution studies are focusing on the stoichiometric perovskite oxide ABO_3 with the ratio of A/B=1, which actually limits the reducible metal to exsolve out that also restricts the overall performance. Recent investigations have indicated the in-situ

exsolution of nanoparticles can be enhanced by controlling the non-stoichiometry of perovskite oxide.[42] By adjusting the perovskite to A/B<1, more cations from B sites will be thermodynamically favored to exsolve out on the surface. The A, O site deficiency may cause an unstable perovskite oxide structure, thus creating a spontaneous tendency for B site exsolution to revert the perovskite to a stable, "defect free" structure. Hence, A-site deficiency is suggested as a new pathway to better decorate the nanoparticles on the oxide surface with more coverage area on the support.

Chapter 3 Experiment Methodology

3.1 Synthesis of Cell Materials

3.1.1 Sol-Gel Combustion Method

The citrate sol-gel combustion method is the main method applied in the experiment for sample fabrication. Sol-gel combustion method is an improved wet chemical method to synthesize nanoparticles with fine homogeneity and lower sintering temperature. It has several advantages such as high purity, good stoichiometric control, ultra-homogeneity with a narrow size distribution, and relatively low processing time and temperature. [43,44]

The sol-gel combustion method is also a type of citric acid & ethylene diamine tetra acetic acid (EDTA) complexing combustion method. As demonstrated by Figure 3.1, the precursor powder is formed by stoichiometric amounts of metal nitrates being dissolved in deionized water with both citric acid and EDTA as co-chelating agents. The metal nitrate and citric acid molar ratio are 1.5:1 while becomes 1:1 for EDTA and metal nitrate. The pH value of the solution is adjusted to 7 to 8 using ammonium hydroxide for a better chelating result. Then the solution is stirred and heated at 80 ºC until the gel is formed. The gel is heated to 300 ºC rapidly and kept for 30 minutes to an hour so that an auto combustion process of the gel will take place to form precursor powder (as-prepared powder). The precursor powders then are ready to be sintered at elevated temperature to form the single phase of targeted perovskite oxide.
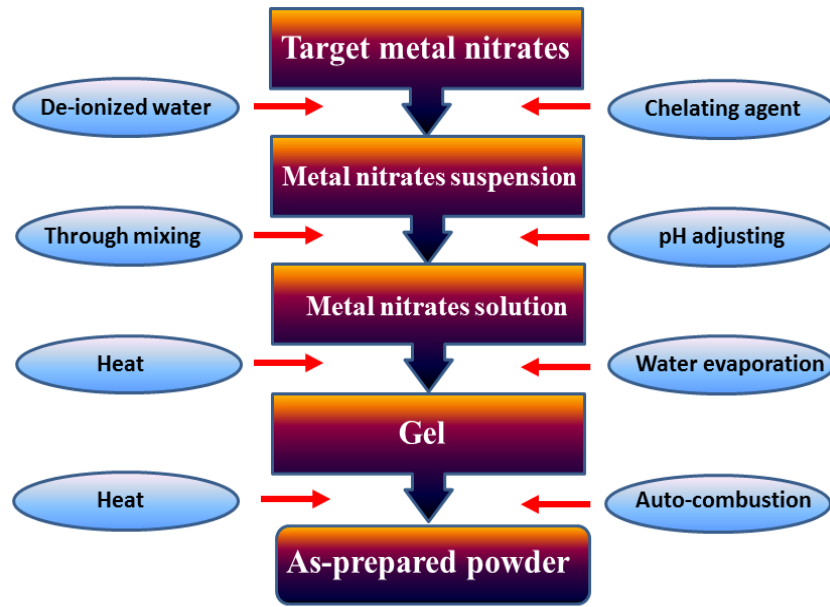
Figure 3.1. Material fabrication flow chart by sol-gel combustion method.

3.1.2 Experimental Procedure of Electrode Fabrication

The main fuel electrode material for this experiment was designed to be 3:1 (molar ratio) Ni-Co bimetallic doped A-site deficient LSC perovskites and be fabricated by in-situ exsolution process. Different bimetallic doping ratios and both A-site deficient and non-deficient perovskites were fabricated and their characteristics were measured. The electrochemical performances of selected cells were tested and compared for SOFC processes.

As mentioned before, the fuel electrodes were fabricated from mixing the stoichiometric amounts of metal nitrates: lanthanum (III) nitrate hexahydrate ($La(NO_3)_3 \cdot 6H_2O$), strontium nitrate anhydrous ($Sr(NO_3)_2$), chromium (III) nitrate nona hydrate ($Cr(NO_3)_3 \cdot 9H_2O$), nickel (II) nitrate hexahydrate ($Ni(NO_3)_2 \cdot 6H_2O$), and cobalt (II) nitrate hexahydrate

$(Co(NO_3)_2 \cdot 6H_2O)$ by the sol-gel combustion method with critic acid monohydrate $(C_6H_8O_7 \cdot H_2O)$ and ethylene diamine tetra acetic acid (EDTA) as the co-chelating agents and the ammonium hydroxide (NH_4OH) solution was applied to balance the pH to 7~8.

The solution was stirred and heated on a heating plate at 80°C until the gel was formed. The gel was placed into a Thermolyne type 6000 furnace to be rapidly heated to 300°C for combustion and the temperature was kept for an hour to finish the precursor powder formation. Then, the precursor powders were collected and milled, and placed into a MTI Type KSL-1700 furnace to be sintered at 1200°C five hours to form a single phase LSC perovskite oxide. LSCF $((La_{0.60}Sr_{0.40})_{0.95}Co_{0.20}Fe_{0.80}O_{3-\delta})$ from Fuel Cell Materials was used as the air electrode in this work.

3.1.3 Fabrication of Solid Oxide Cells

The electrode ink is fabricated by mixing the electrode material powders with the electrode glue (in alpha-terpinol mixed with 10% polyethylene glycol) using a ball milling machine (Figure 3.2). Then the well-mixed electrode ink will be printed on each side of the electrolyte pellets by a screen printer as shown in Figure 3.3. The ink printed cell will be sintered at elevated temperature to form a compact contact between the electrode and electrolyte. After sintering, Au paste is painted on both sides of the cell as the electrode current collectors.
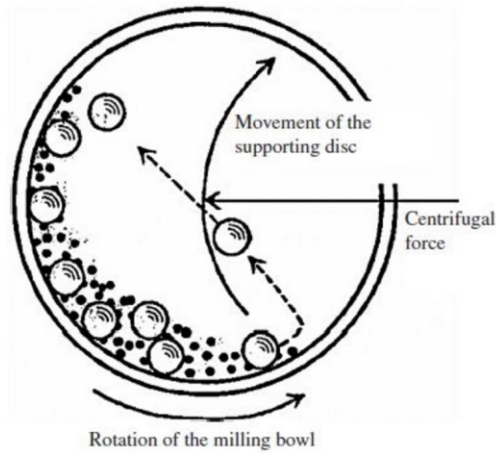
Figure 3.2. Schematic of Milling Machine.[45]
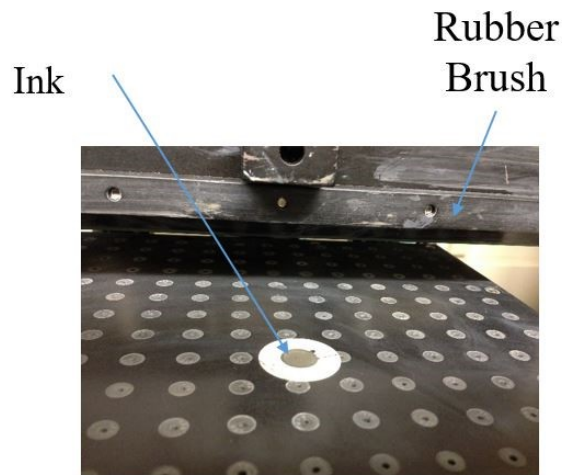
Figure 3.3. Image of the screen printer and ink printed cell.

Electrode ink was fabricated by thoroughly mixing the electrode powder, the GDC10 power (10% gadolinium doped) and the electrode glue at the weight ratio of 1.5:1.5:1.7 in the milling machine for 2 hours. The GDC buffer layers introduced at the electrode and electrolyte interfaces were made by mixing the GDC10 powder with the electrode glue at 1.7:3 weight ratios. Buffer layers were painted at the two sides of the electrolyte, the 25 mm diameter and 0.25 to 0.3mm thickness 8 mol% yttria doped YSZ substrate from Fuel

Cell Materials. Buffer layers were dried in an air-drying oven and sintered with the electrolyte at 1300°C for 5 hours. Then fuel electrode ink was painted on one side of the buffer layer with the painting area of 0.965 cm^2. After air drying the ink, the fuel electrode LSC was sintered at 1200°C for 5 hours. The air electrode LSCF was painted last, on the other side of the buffer layer with the same area as the fuel electrode. Then the dried air electrode was sintered at 950°C for 4 to 5 hours in the furnace to obtain good bonding between the electrode and electrolyte. Au paste was painted on both sides of the electrode as the current collector.

3.2 Electrochemical Test Setup for SOFC

The well fabricated cells were placed in an electrochemical test setup as shown in Figure 3.4, to be ready for electrochemical performance tests. The fabricated cell is sealed on a coaxial alumina two-tube setup by a ceramic sealant (Ceramabond 552, Aremco Products) to separate air and fuel gas on both sides of the electrolyte. The current collectors for the two electrodes are connected to the electrochemical workstation (potentiostat) by 0.5 mm diameter silver wires with silver paste. Two volumetric flow meters are inserted into the system to regulate the flow rate of inlet gases, and the outlet gases flowing at the cathode and anode are removed from the system to carry away the generated products and thus allow the reaction to continue. Once the ceramic sealant is cured, the set up will be placed at elevated temperature on the Thermolyne tubular furnace untill it has risen to a certain operating temperature. The electrochemical workstation is used to measure and collect data and measure the produced power from SOFC operations.
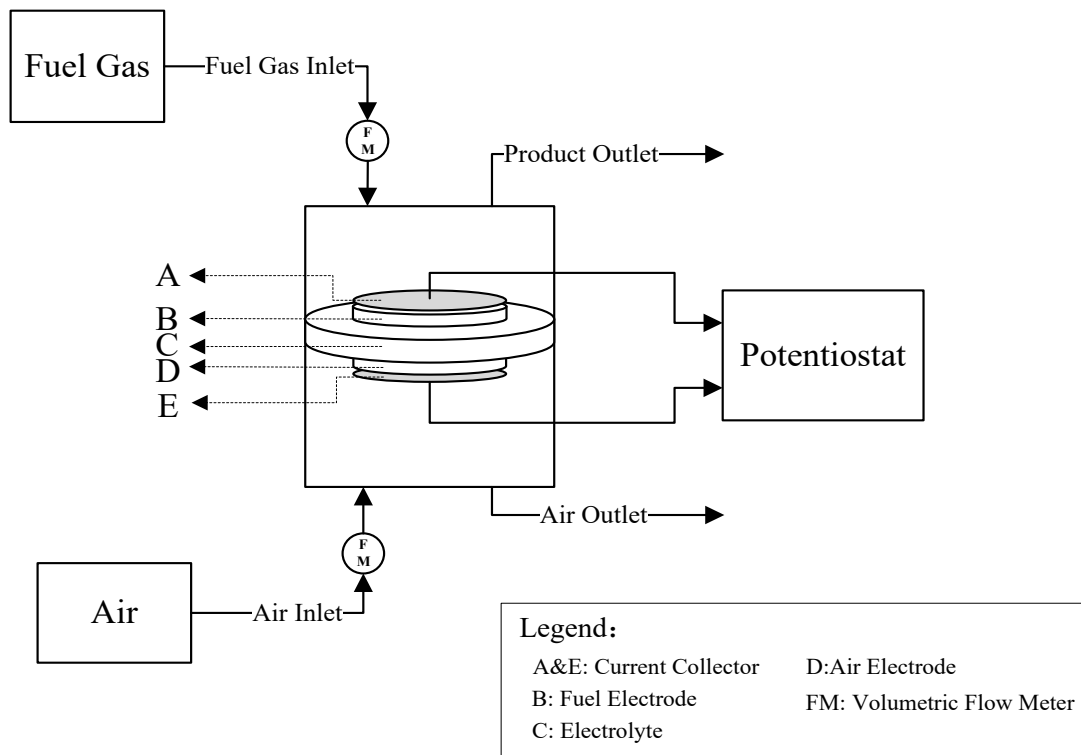
Figure 3.4. Schematic Diagram for electrochemical performance test setup.

3.3 Characterization of the Catalyst

3.3.1 Powder X-Ray Diffraction

The phase formation of the catalyst is analyzed by powder X-Ray diffraction (XRD) by using a Rigaka D/max-2500 X-ray diffractometer with a Cu Kα radiation at room temperature and the data are analyzed through Jade and Xpert Highscore Plus Software. As well as identifying the phase formation of the material, lattice parameters, lattice defects and grain size of nanoparticles can also be identified by the XRD test. During the test process, the cleavage phase of sample crystals appears to reflect the X-ray beam at a certain angle of incidence, θ. When the incident X-ray beam has the wavelength of λ and the distance between the atomic layers of the crystal is represented by variable d, the X-ray

wave interface of a sample is described by Bragg's Law, equation 10, where n is an integer.[46]

$$n\lambda = 2d \sin\theta \quad (10)$$

3.3.2 Scanning Electron Microscopy and Energy Dispersive X-ray Spectroscopy

Scanning electron microscopy (SEM) is a powerful technique that produces images of the sample surface morphology by electron scanning. During the operation process, while a focused beam of electrons is scanning the surface, electrons will interact with sample atoms and produce various signals such as secondary electrons (SE) and backscattered electrons (BE) that contain the information about the surface image and compositions of the sample.[47] Gold or carbon coatings are usually required to be applied onto the sample surface to produce extra conductivity to the sample. Some SEM equipment also contains an energy dispersive X-ray spectroscopy (EDS) system to use x-ray fluorescence to specify the elemental compositions as well as detailed component concentrations. In this research, the microstructure and morphology of catalysts, cross section and surface images of cells as well as the material composition by EDS analysis are obtained at room temperature by Zeiss Sigma 300VP-FESEM equipment.

3.3.3 Thermogravimetric Analysis and Mass Spectrometry

Thermogravimetric analysis (TGA) is a method of thermal analysis that can measure the changes in chemical and physical properties of the sample as a function of temperature and as a function of time. The sample's heat change and/or weight loss during the process are measured with a constant heating rate or constant operating temperature; thus it reveals the change in chemical phenomena of the sample including decomposition, dehydration, reduction and oxidation processes. The inlet pipe of the mass spectrometer (MS) is usually

connected with the gas outlet flow of the TGA to analyze the change of gas composition during the TGA operation as a function of time/temperature. MS provides an electromagnetic field inside that can characterize different mass and charge properties of ionized sample particles inside in order to identify the sample chemical compositions. In this research, TGA, SDT Q600 (TA instrument), is mainly applied for the metal nanoparticle exsolution and oxygen nonstoichiometric analysis as well as the temperature program oxidation (TPO) process with the MS measurement, thermostat QMS 200, at a heating rate of 10 ºC min^{-1} from room temperature to 900 ºC.

3.3.4 Gas Chromatography

Gas chromatography (GC) is one of the most widely used techniques for analyzing the gas components without decomposition. The GC carrier gas, usually an inert gas, is the mobile phase and the immobilized polymeric liquid is usually applied as the stationary phase in the equipment. The carrier gas needs to be subsequently supplied from the inlet stream that continuously flows through the whole column and into the component detector. The sample gas is injected into the injection port and gets carried into the column by a carrier gas, and gets separated inside the column based on different solubility and relative vapor pressures of the components in the stationary and mobile phases. As the analytes pass into a detector with a carrier gas, their different physicochemical properties are detected and generated as electronic signals to measure the specified amount of different components present.[48] GC has a wide range of operating temperature from 5°C to 400°C, wide range of component detection and a good repeatability of the measurement. In this research, GC is mainly applied for the hydrogen-temperature program reduction (H$_2$-TPR) analysis using a Hewlett Packard 5890 Series II gas chromatograph.

3.4 Electrochemical Measurements

The electrochemical performance test of this research is investigated by using the electrochemical workstation of a Solartron 1287 potentiostat and a Solartron 1255 frequency response analyzer.

3.4.1 Electrochemical Impedance Spectra

Electrochemical impedance spectroscopy (EIS) is a technique that determines the energy storage and dissipation properties over a range of frequencies by measuring the impedance, which refers to the frequency dependent resistance to current flow of a circuit element. Impedance spectroscopy will impose a potential perturbation on the testing cell and then measure and collect the current output. Therefore, the impedance is described by the following equation (11), where Z_ω, E_ω and I_ω are the frequency dependent resistance (impedance), frequency dependent potential and frequency dependent current, respectively.[49]

$$Z_\omega = E_\omega / I_\omega \ (11)$$

For solid oxide cells, the EIS process is essential for cell performance detailed analysis. It provides a significant pathway to distinguish the cell performance consequences from different losses and polarization processes. Figure 3.5 is a typical EIS diagram, Nyquist plot which is usually used for SOFC analysis. The x-axis and y-axis indicate the values of real impedance and imaginary impedance, respectively, and the frequency value decreases with increasing x-axis value. In general, three types of losses that contribute to the arcs appear in the diagram as the overpotential of the cell at a given current density. The first one is the ohmic losses, shown as the curve's first intercept with the x-axis, which is mainly contributed by the resistance of electrolyte material; resistances of electrode materials and interconnects also make minor effects. The activation polarization losses are caused by the

operating activities of the two electrode materials, which is expressed by the two large arcs at the high to middle range of the frequency. In the low-frequency range, the linear line is expressing the resistance domains due to mass transfer effects due to the diffusion difficulty.[50] A frequency range of 10^6 Hz to 1 Hz is applied in this experiment impedance spectra measurement with required AC perturbation.
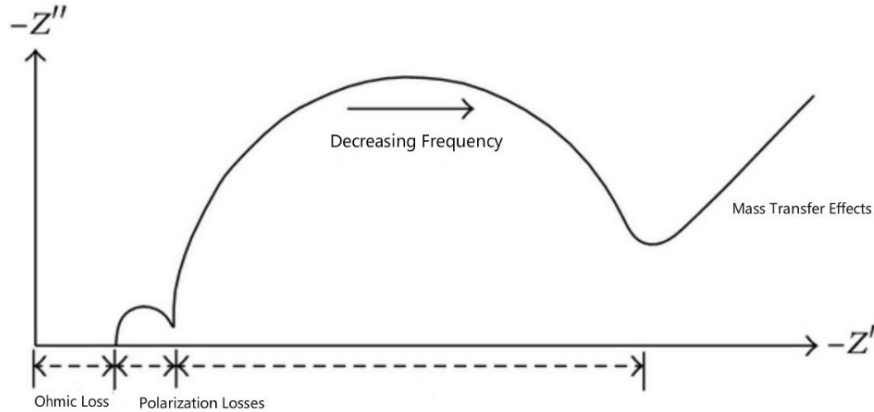
Figure 3.5 Schematic of a typical Nyquist plot for EIS analysis for SOFC.[50]

3.4.2 Current Density-Voltage Curves

The voltage (V) versus current density (j) curve is used to analyze the electrochemical performance of the cell by plotting the change in voltage-current relationship during the operation process, which is also called as the j-V curve. For SOFCs measurement, the j-V curve is usually measured at the potential dynamic mode whereby the workstation will control the various voltage values in the system and record the corresponding current density values. For SOFC tests, the voltage will vary within the range from OCV to zero at 5 millivolts per second (mVs^{-1}) or 10 mVs^{-1} rates. After collecting the current density data with corresponding voltage values, the produced power density (P) from the SOFC will be acquired by multiplying voltage and current density values as shown in equation

12. For a standard j-V curve, the current density (mA/cm^2) is the x-axis and the voltage output (V) and power density (mW/cm^2) are the two y-axes on the diagram. In this experiment, the potential static mode is also applied for SOFC tests, that makes the cell operate under a constant voltage value and deducts the current stability performance as a function of time. Therefore, the stability test diagram will have the current density value on the y-axis and time will be the x-axis.

$$P = Vj \quad (12)$$

Chapter 4 Results and Discussion

4.1 Analyses of Fuel Electrode Materials

The strontium doped lanthanum chromite based perovskite oxide was designed to be 30 mol% Sr doped at the A-site with 10 mol% La A-site deficiency and bimetallic B-site doping was designed to starts from 15 mol% based on the previous experiment results from our group. Thus, the first step of experimental designation for bimetallic doping ratios is shown in Table 4.1.

Table 4.1. Designation of Bimetallic Doping Ratio Experiment.

Abbreviation	Composition
LSC-6315NiCo	$(La_{0.6}Sr_{0.3})(Cr_{0.85}NiCo(3:1)_{0.15})O_{3-\delta}$
LSC-6312NiCo	$(La_{0.6}Sr_{0.3})(Cr_{0.88}NiCo(3:1)_{0.12})O_{3-\delta}$
LSC-6309NiCo	$(La_{0.6}Sr_{0.3})(Cr_{0.91}NiCo(3:1)_{0.09})O_{3-\delta}$
LSC-6306NiCo	$(La_{0.6}Sr_{0.3})(Cr_{0.94}NiCo(3:1)_{0.06})O_{3-\delta}$
LSC-6303NiCo	$(La_{0.6}Sr_{0.3})(Cr_{0.97}NiCo(3:1)_{0.03})O_{3-\delta}$

In order to successfully accomplish the in-situ exsolution process of doped active nanoparticles, the formation of the single phase (pure phase) LSC perovskite oxide structure after sintering is necessary. The phase structures of the synthesized materials were characterized by XRD with Cu Kα radiation scanned from 20º to 80º (2θ) at 2º per minute. The XRD patterns of freshly fabricated materials (Table 4.1) are shown in Figure 4.1.
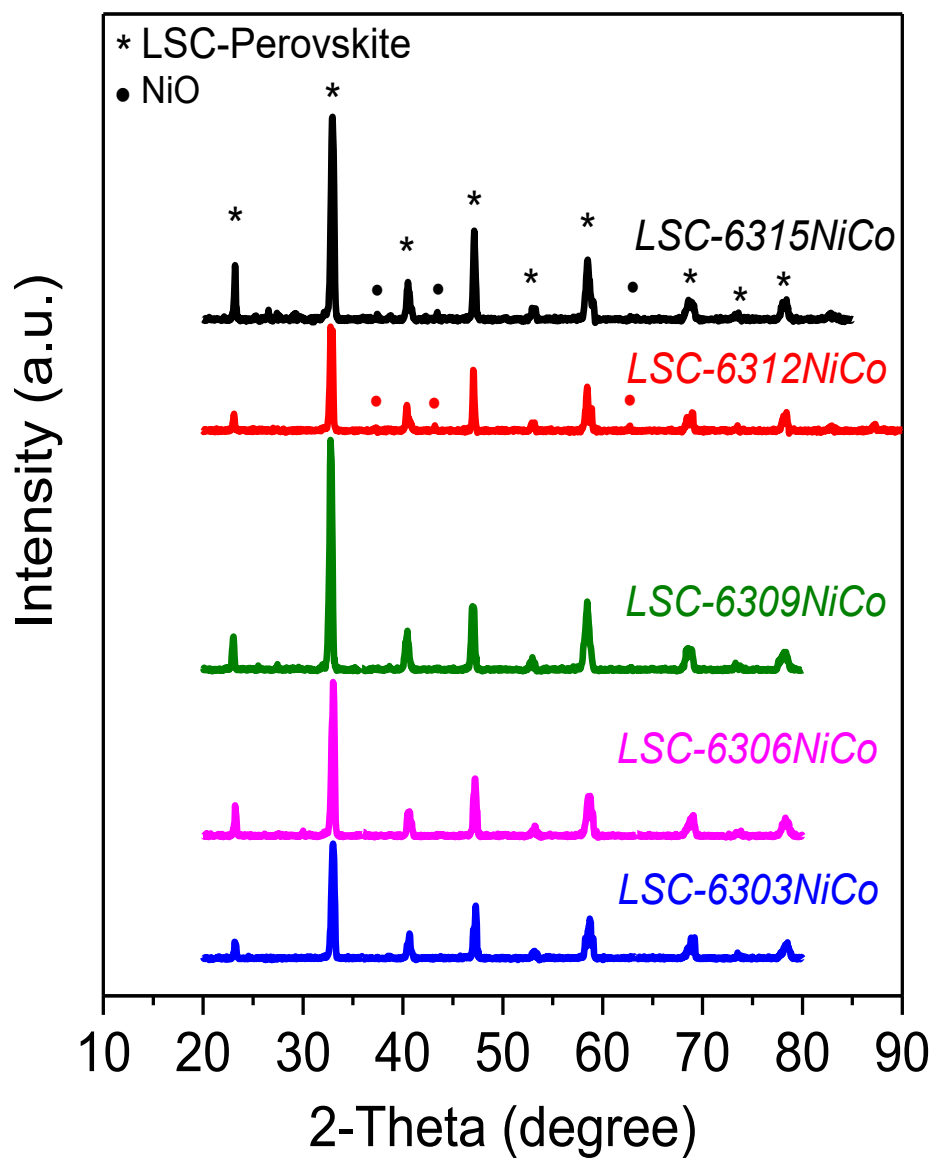
Figure 4.1. Crystalline structures of LSC based perovskite with different bimetallic doping ratios: LSC-6315NiCo LSC-6312NiCo LSC-6309NiCo LSC-6306NiCo LSC-6303NiCo.

The 9 starred (*) peaks around 2θ equals to 23º, 32º, 40º, 47º, 53º, 58º, 68º, 73º and 78º marked in the diagram are the peaks matches with the main LSC structure, which exhibits a perovskite structure with orthorhombic phase unit cells. As revealed in the figure, LSC-6309NiCo, LSC-6306NiCo, and LSC-6303NiCo have shown the single-phase perovskite oxide in the XRD diagram, which means the B-site doping of the A-site deficient LSC base does not have any influence on the crystalline structure of the perovskite oxide. However, the diffraction peaks at around 2θ equal to 37º, 43º and 63º, the dot (·) marked peaks, were detected for both LSC-6315NiCo and LSC-6312NiCo perovskite oxides. These peaks are the main peaks for the nickel oxide (NiO) phase (reference code 01-089-7131); thus the appearance of these peaks represents the formation of NiO phase in the sample materials. The formation of NiO indicated the doping saturation of pure phase LSC perovskites with 15 mol% and 12 mol% of bi-metal doping into B-site positions of LSC base. As the result, in this experiment, the limitation of B-site doping ratio for A-site deficient LSC perovskite oxide is determined as up to 9 mol%. The change of tolerance factor t is a possible reason that affects the transition metals' doping limitations. The B-site doped Ni and Co increase the B-site ionic radius that decreases the tolerance factor t and decreases the structure stability.

Based on the maximum doping limitation obtained from Figure 4.1, different compositions of fuel electrodes were fabricated, which were the B-site bimetallic doped A-site deficient perovskite oxide, B-site monometallic doped A-site deficient perovskite oxide, and the B-site bimetallic doped non-deficient perovskite oxide, as listed in Table 4.2.

Table 4.2. Designation of fuel electrode compositions.

Abbreviation	Composition
LSC-6309NiCo	$(La_{0.6}Sr_{0.3})(Cr_{0.91}NiCo(3:1)_{0.09})O_{3-\delta}$
LSC-6309Ni	$(La_{0.6}Sr_{0.3})(Cr_{0.91}Ni_{0.09})O_{3-\delta}$
LSC-7309NiCo	$(La_{0.7}Sr_{0.3})(Cr_{0.91}NiCo(3:1)_{0.09})O_{3-\delta}$

The phase structures of these materials were also characterized by XRD with Cu Kα radiation scanned from 20º to 80º (2θ) at 2º per minute. The XRD results are shown below in Figure 4.2. Figure 4.2 a) is the general XRD diagram for perovskite oxides $(La_{0.6}Sr_{0.3})$ $(Cr_{0.91}NiCo (3:1)_{0.09})$ $O_{3-\delta}$ (LSC-6309NiCo), $(La_{0.6}Sr_{0.3})$ $(Cr_{0.91}Ni_{0.09})$ $O_{3-\delta}$ (LSC-6309Ni), and $(La_{0.7}Sr_{0.3})$ $(Cr_{0.91}NiCo (3:1)_{0.09})$ $O_{3-\delta}$ (LSC-7309NiCO) respectively. Figure 4.2 (b) is the detailed peak positions of the 32° main peak for LSC-6309NiCo, LSC-6309Ni and LSC-7309NiCo, respectively.
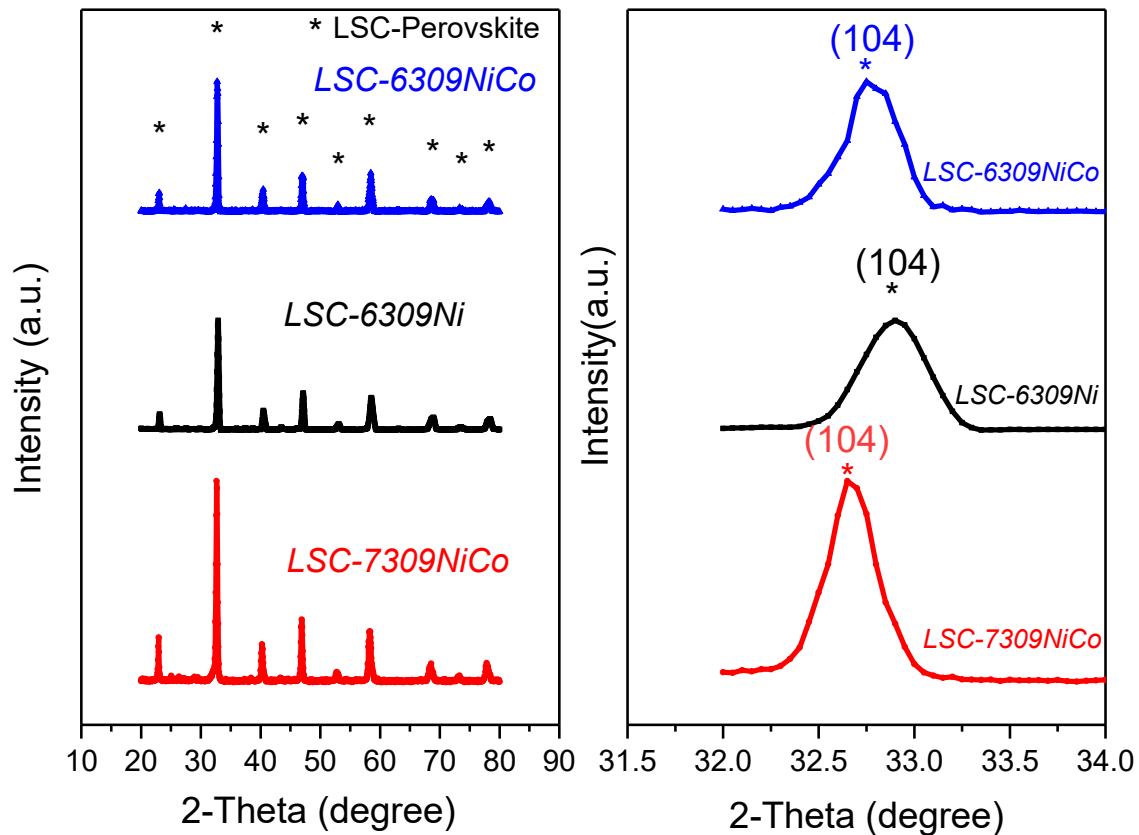
Figure 4.2. XRD diagram for perovskite oxide LSC-6309NiCo LSC-6309Ni and LSC-7309NiCo a) the general diagram for all peaks b) detailed positions for main peaks.

As illustrated by the peaks in Figure 4.2 a), all of the LSC-6309NiCo, LSC-6309Ni and LSC-7309NiCo compositions had successfully formed the single phase of LSC perovskite oxide as marked by the stars (*). This result verifies the appropriate accommodation of the metal-substituted in the B-site of LSC perovskite base at 9 mol% for both chemical stoichiometry and non-stoichiometry situations as well as the bimetallic and monometallic doping situations. Moreover, some minor shifts in the structure could be identified by analyzing in detail the position of the XRD peaks. The highest intensity (main) peaks, (104) peaks, for LSC-6309NiCo, LSC-6309Ni and LSC-7309NiCo are expressed in Figure 4.2

b) to represent the peak shifting tendency. Even though the perovskite structure of doped LSCs presented in Figure 4.2 a) are in pure orthorhombic phase unit cells, the (104) peak of the unit cell had been shifted due to different doping compositions. The (104) peaks for LSC-6309NiCo, LSC-6309Ni and LSC-7309NiCo were at 32.75°, 32.85°, and 32.65° (2θ), respectively. This slight shift of the peaks can be analyzed by the Bragg Law (equation 10). Since $n\lambda = 2d\sin\theta$, that with the nλ unchanged, the larger value of 2θ corresponds to a smaller value of d, which means smaller unit cell volumes. Thus, according to the Figure 4.2 b), LSC-6309Ni should have the smallest cell volume while LSC-7309NiCo has the largest. The changes of cell volume sizes for LSC-6309NiCo, LSC-6309Ni and LSC-7309NiCo can be explained from the B-site substitutions and A-site non-stoichiometry. The ionic radii for 6-fold coordination B-site Cr^{3+}, Ni^{2+} and Co^{2+} are 0.615Å, 0.69Å and 0.745Å respectively.[51] Thus the bimetallic Ni-Co doping has increased the unit cell volume compared to single Ni doping. Also, the decrease of the unit cell volume of LSC-6309NiCo compared with LSC-7309NiCo is mainly caused by the A-site cation non-stoichiometry, which is in agreement with the literature results of A. V. Kovalevsky et al.[52]

4.2 In-situ Exsolution Analysis

With the doping of Ni-Co metal at the B-site of LSC, the in-situ exsolution phenomena are expected to occur during the reduction process by H_2. The in-situ exsolved nano metal particles are the key points for improving the LSC electrochemical catalytic activity. With in-situ exsolution, the metallic particles are expected to be small in size (nanoscale) and uniformly decorated on the surface of the LSC base with metal phases. The mechanism of the exsolution of metal particles can be partially explained by the Gibbs free energy. The values of Gibbs free energy of the reduction reaction of each cation were calculated using HSC 6.0 software. Figure 4.3 depicts theoretical Gibbs free energies for different metal oxides that are involved in this experiment. Only Co_3O_4 and NiO shall be the reducible

element under the high temperature from 600°C to 900°C since only Co_3O_4 and NiO have contained negative Gibbs free energies. At 800°C, Co_3O_4 has a -256.91kJ Gibbs free energy and NiO has -46.646kJ, while all other elements have kept positive values. In addition, based on the value of Gibbs free energy, Co_3O_4 shall has a higher reducibility than NiO.
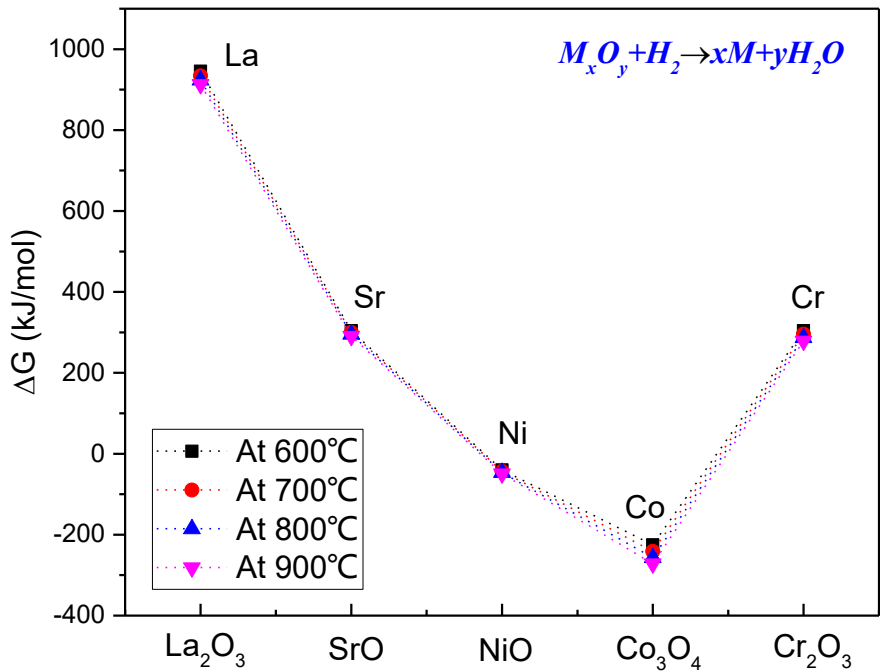
Figure 4.3. The theoretical value of Gibbs free energy for reduction of each element oxide in LSC-6309NiCo perovskite at 600 ∘C to 800 ∘C.

The exsolved Ni and Co metallic particles are expected to form a solid solution as Ni-Co alloy phase during the reduction process. Theoretically, it is known that Co and Ni are adjacent to each other in the periodic table that satisfies the Hume-Rothery rule[53] which indicates they can easily form a solid solution phase (alloy) with various ratios. Ni and Co. The Ni-Co phase diagram in Figure 4.4 [54] also indicates this point. As shown in the phase

diagram, the Ni-Co alloy could be formed at any composition at the experimental temperature of 850°C. Thus, it is tentatively suggested that the formation of Ni-Co alloy during the exsolution process in this experiment is favorable.
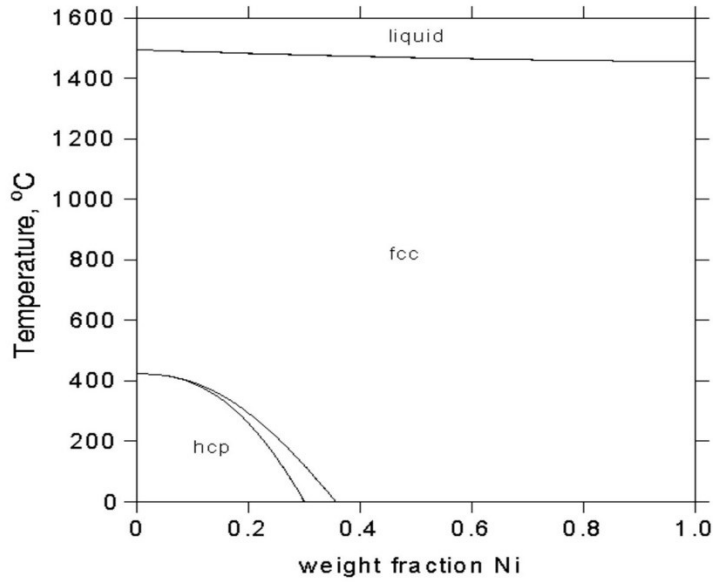
Figure 4.4. Ni-Co alloy phase diagram.[54]

4.2.1 XRD Results Analysis

After successfully fabricating the bimetallic doping perovskite oxide electrodes, these electrodes were placed into the MTI-type GSL 1100X tube furnace to be reduced at 800°C for 3 hours with $5\%H_2/N_2$ reducing atmosphere. The doped nano metal particles should be in-situ exsolved out of the bulk LSC and get uniformly dispersed on the surface. In this experiment, characterization of the in-situ exsolved nanoparticles were examined by XRD, TPR TGA and SEM analysis.

The XRD diagram for reduced LSC-6309NiCo, LSC-6309Ni and LSC-7309NiCo, and their detailed exsolution peak positions are illustrated in Figure 4.5 a), b) and c). All of LSC-6309NiCo LSC-6309Ni and LSC-7309NiCo have successfully maintained the main LSC structure after the high temperature reduction process as indicated by star marked peaks in the diagram. The diffraction peak at 2θ equals to $44.6°$ has been detected for LSC-6309Ni. This peak agrees with the theoretical XRD position for pure metal Ni at 2θ equals 44.605 (reference number 01-070-0989), which confirms the metallic nanoparticles in-situ exsolution process. In addition, a clear diffraction peak at 2θ equals to $\sim44.5°$ has been detected for both R-LSC-6309NiCo and R-LSC-7309NiCo perovskites in Figure 4.5 b) & c). These peaks are believed to be the in-situ exsolved Ni-Co alloy phase from the perovskite because this position is exactly in between the main peaks of metallic Ni and Co, which are at 2θ equals $44.605°$ and $43.801°$, respectively, with 100% intensity. By overlapping the diffraction peaks for LSC-6309NiCo, LSC-6309Ni and LSC-7309NiCo in Figure 4.5 c), the peak shifting tendency from Ni to Ni-Co alloy is clearly exhibited. The exsolution peak for chemically stoichiometric LSC-7309NiCo in Figure 4.5 c) is not distinct enough due to the lack of exsolution from A-site deficiency. The diffraction peak for LSC-6309NiCo has clearly shifted toward the left compared with the one for LSC-6309Ni in Figure 4.5 c), which are at $44.5°$ and $44.6°$ (2θ) respectively. As mentioned before, this bias is likely caused by the existence of the Ni-Co alloy phase instead of pure metal Ni phase exsolved from the perovskite structure during the exsolution process.
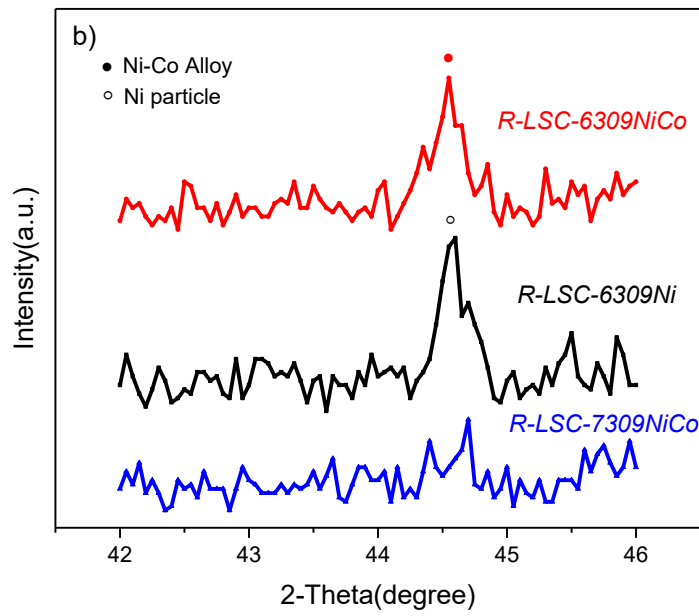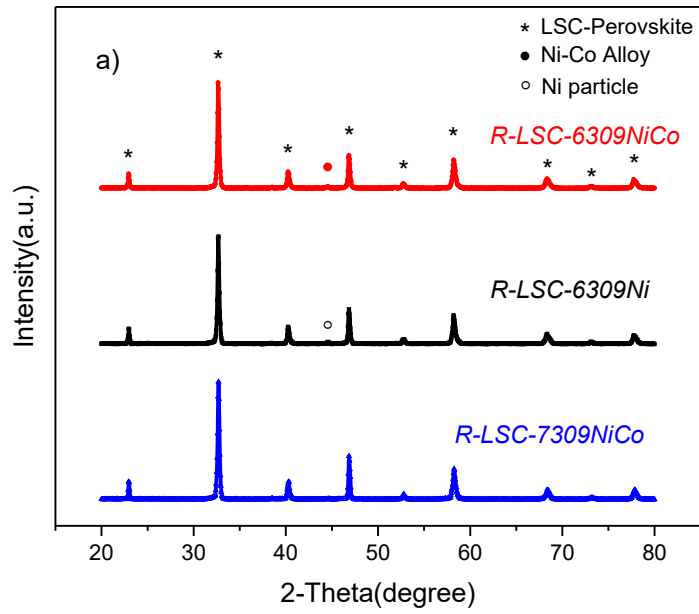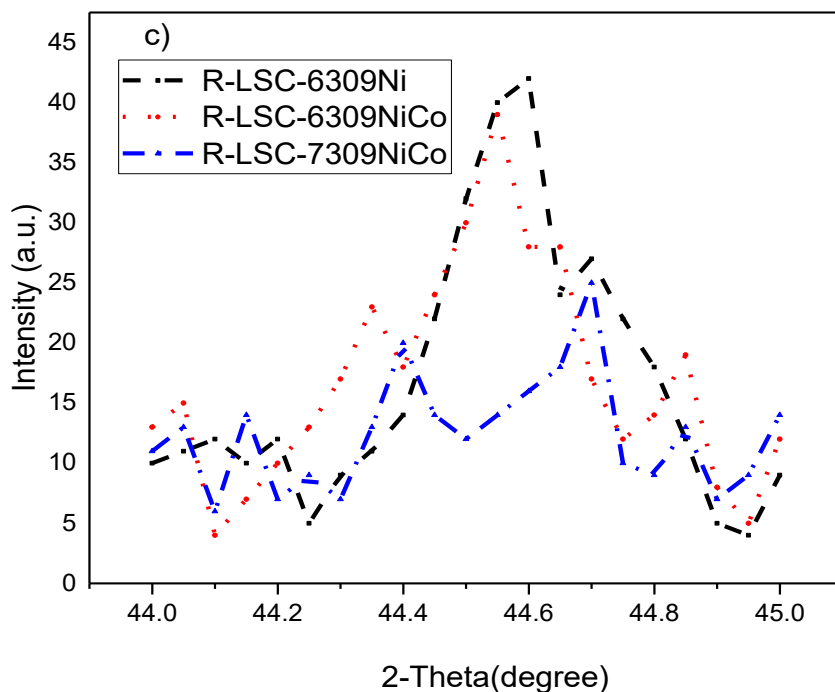
Figure 4.5. a) XRD diagram for reduced LSC-6309NiCo LSC-6309Ni LSC-7309NiCo b) specified diagram for exsolution peaks c) overlapping of exsolution peaks.

The XRD diagram for reduced LSC-6309NiCo, LSC-6306NiCo and LSC-6303NiCo electrodes and their detailed metal exsolution peaks are revealed by Figure 4.6 a) and b), respectively. Similar to the LSC-6309NiCo perovskite, both LSC-6306NiCo and LSC-6303NiCo perovskites are in stable LSC base structures that have been perfectly maintained under the high temperature reduction atmosphere. LSC-6306NiCo has a clear diffraction peak at 2θ equals to 44.5°, which is at the same position as the LSC-6309NiCo's diffraction peak in Figure 4.6 a) & b). This peak is considered as the in-situ exsolved Ni-Co alloy phase from the perovskite; as discussed before measured peaks are slightly shifted towards the lower degrees of 2θ compared with pure Ni metal due to the generation of Ni-Co alloy. LSC-6303NiCo perovskite does not likely have any obvious exsolution peak

44

through XRD, which might be caused by the low doping amount of Ni and Co into the structure.
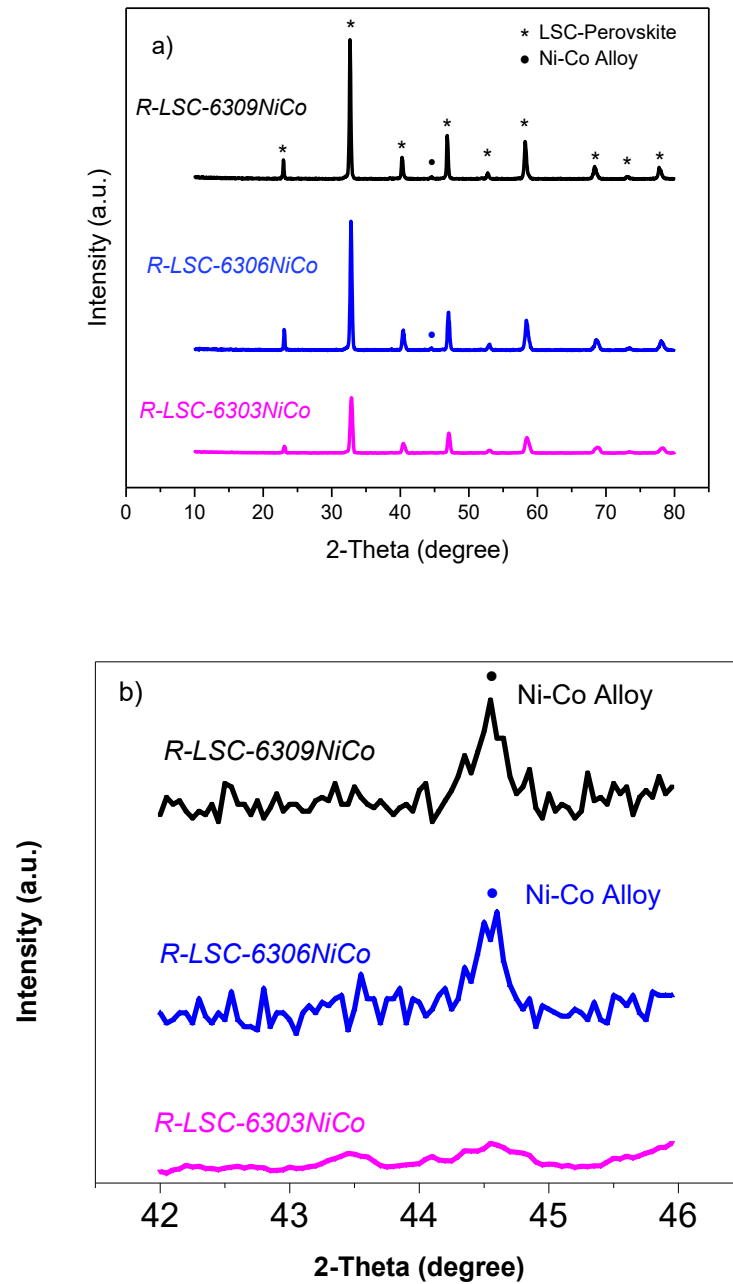
Figure 4.6. a) XRD diagram for reduced LSC-6309NiCo LSC-6306NiCo LSC-6303NiCo b) specified diagram for Ni-Co alloy peaks.

4.2.2 TPR Results Analysis

To investigate the reducibility of this series of bimetallic doped A-site deficient LSC perovskite oxides and the synergistic effect between Co and Ni, hydrogen temperature programmed reduction (H_2-TPR) tests were carried out, and the corresponding results are plotted in Figure 4.7. This technology was achieved by an AutoChem II 2920 instrument (Micromeritics, USA) equipped with a thermal conductivity detector. All samples were treated with helium at 1000 °C for 30 min before H_2-TPR. The flow rate for this analysis was 10% H_2/Ar at 10 mL per minute, and the temperature ramping rate was 10 °C per minute.
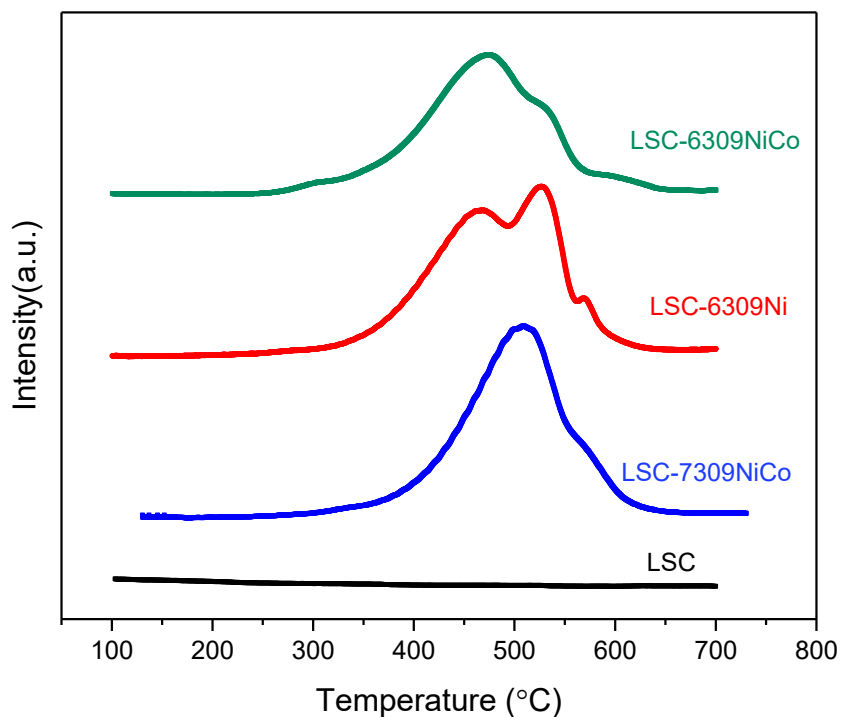
Figure 4.7. H_2-TPR curves of the fresh LSC, LSC-6309NiCo, LSC-6309Ni, and LSC-7309NiCo.

There is no obvious peak that occurred in the pattern of LSC perovskite oxide as denoted in Figure 4.7. This result indicates that $La_{0.7}Sr_{0.3}CrO_{3-\delta}$ might not have exsolved nanoparticles in a reducing atmosphere with increasing temperature. This result is consistent with the Gibbs free energy diagram as mentioned before. Doping of active metals Ni and Co has made a great improvement on LSC's reducibility. Clear H_2 consumption peaks are observed for both LSC-6309NiCo and LSC-6309Ni (Figure 4.7) compositions, which show multiple peaks of different Ni/Co states. The curve of LSC-6309Ni has two clear H_2 consumption peaks at ~470 °C and 530 °C. Based on previous studies[55,56], the first peak (α peak) of LSC-6309Ni indicates the reduction of Ni ions from Ni^{3+} to Ni^{2+} (around 500°C), while the second peak (β peak) represents the reduction from Ni^{2+} to metallic Ni^0 (before 600°C). The Ni^{2+} to Ni^0 transformation consumes the highest amount of hydrogen that can be confirmed from the intensity of the β peak. LSC-6309Ni had a third small peak at around 570°C, which is considered to be the LSC structure H_2 consumption peak. The Co doping effect on reducibility is analyzed based on the different peak shapes between LSC-6309NiCo and LSC-6309Ni. The LSC-6309NiCo material has a similar shape of α peak at ~470°C, but with a much lower β peak at 510°C. This phenomenon indicates that the formation of the Ni–Co solutions significantly changes the reduction behavior of Ni oxide. A previous study indicated that the main H_2-TPR peak for Co_3O_4 occurs at 433°C, which just overlapped with α peak of Ni.[57] That can also explain the wider range of α peak in LSC-6309NiCo than LSC-6309Ni. The β peak for LSC-6309NiCo has moved to a lower temperature and got partially merged with the α peak. With the help of XRD results for metal exsolution of reduced samples, the exsolution process of Ni-Co alloy can be inferred as having similar reducibility with Ni metal but requires a lower temperature. The LSC-7309NiCo has α peak at around 500°C, and a really weak β peak before 600°C. This result means that the exsolution process of LSC-7309NiCo

requires higher energy than LSC-6309NiCo for both Ni^{3+} to Ni^{2+} and Ni^{2+} to Ni^0 transformations. In addition, the weak β peak in the LSC-7309NiCo curve has verified the small number of nanoparticles exsolved out of the surface, which fits the result indicated by XRD in Figure 4.5. In conclusion, this TPR result clearly indicates that the addition of the second metal Co can significantly manipulate the reduction behavior of Ni nanoparticles. Also, the existence of A-site deficiency could facilitate the reduction of Ni^{2+} to metallic Ni to generate more Ni-Co nanoparticles.

The results of H_2-TPR for LSC-6306NiCo and LSC-6303NiCo are plotted in Figure 4.8; LSC and LSC-6309NiCo curves are provided for comparison purposes. LSC-6306NiCo TPR curve is observed to have almost the same pattern as the LSC-6309NiCo curve that the α peak is merged with the β peak at a temperature of 470°C and 510°C, respectively. LSC-6303NiCo has a strong α peak at 470°C but no clear β peak at a higher temperature. This result indicates that most of the hydrogen-consuming process for LSC-6303NiCo is about the Ni^{3+} to Ni^{2+} transformation but not too much for metallic phase formation. This is due to the small bimetallic doping amount for LSC-6303NiCo, and the low exsolution amount agrees with the XRD peaks of reduced LSC-6309NiCo in Figure 4.6.
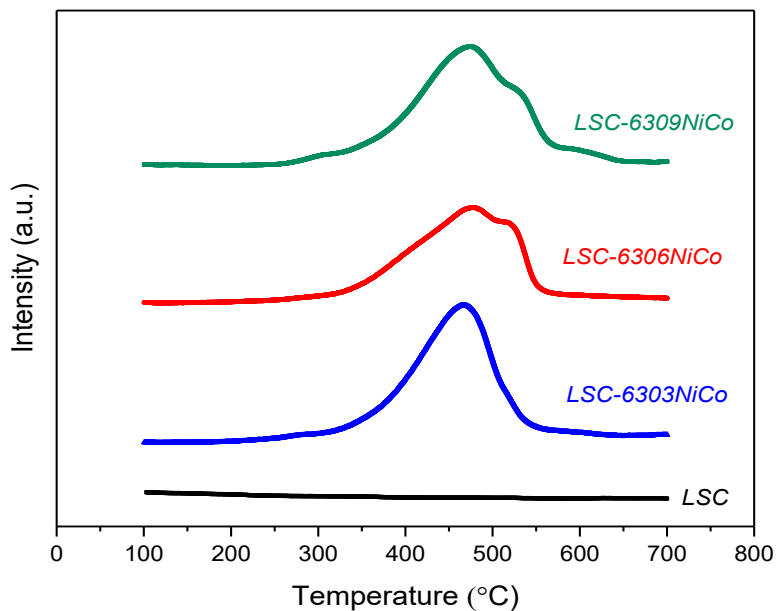
Figure 4.8. H2-TPR curves of the fresh LSC, LSC-6309NiCo, LSC-6306NiCo, and LSC-6303NiCo.

4.2.3 TGA Results Analysis

As the in-situ exsolution of metal oxides causes the metal ions to be reduced at the bulk surface, some correlated lattice oxygen ions escape from the LSC perovskite oxide as well. The shortage of oxygen ions has introduced fair amount of oxygen vacancies (δ) into the structure. Oxygen vacancies play a significant role in the ionic conductivity and electrochemical catalytic activity of a perovskite material. In this experiment, the TGA was performed to measure the material weight losses of the materials with increasing of temperature in the reducing atmosphere. As stated by previous studies, the primary weight loss in the curve is due to the formation of oxygen vacancies.[52,58,59] The TGA was operated for different materials from 100°C to 850°C at a heating rate of 20 °C per minute in 5% H_2/N_2. The TGA diagram for LSC-6303NiCo, LSC-6306NiCo, and LSC-6309NiCo are

depicted in Figure 4.9 a). Figure 4.9 b) contains the TGA curves for LSC-6309NiCo, LSC-6309Ni, and LSC-7309NiCo.
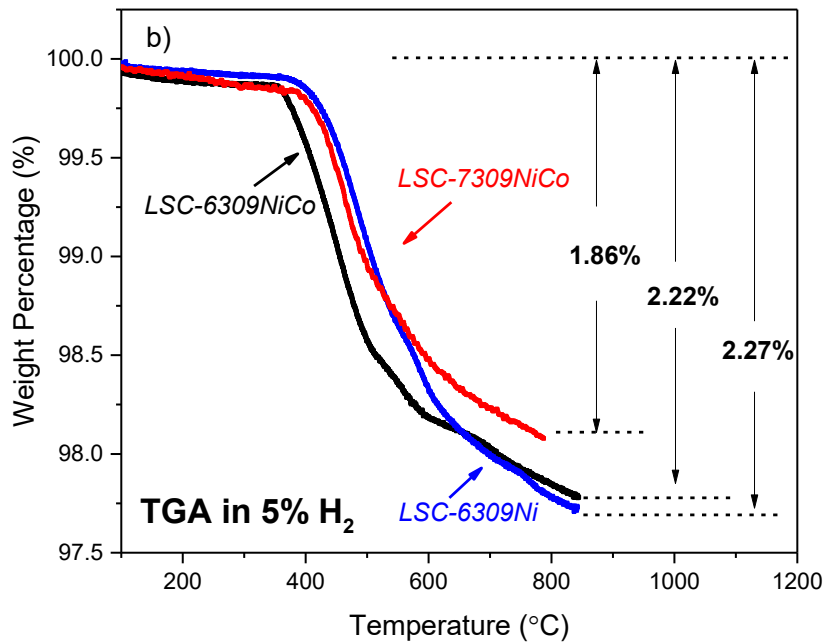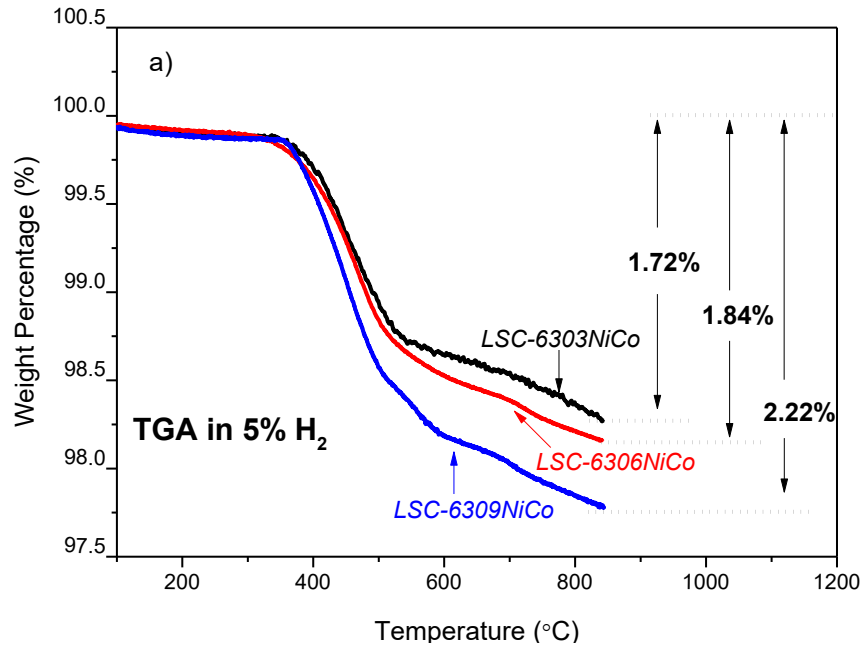
Figure 4.9. TGA diagram in 5%H$_2$/N$_2$ for a) LSC 6303NiCo, LSC-6306NiCo, and LSC-6309NiCo b) LSC-6309NiCo, LSC-6309Ni, and LSC-7309NiCo.

All the curves in Figure 4.9 a), LSC-6309NiCo, LSC-6306NiCo, and LSC-6303NiCo have shown three stages of change in the TGA diagram. The first stage is from 100°C to 380°C that all curves have gradual decreasing tendencies, which could be understood as the loss of adsorbed water.[60] When the temperature goes higher than 380°C, all curves become sharp and keep dropping at their largest slope until around 500°C was reached. The TGA curves for tested materials have shown slightly different ending temperatures for the second stage. LSC-6303NiCo has an ending temperature at 520°C, while both LSC-6309NiCo and LSC-6306NiCo are around 480°C. The third stage of the curves is from 500°C to 850°C until the end of the test. All three curves have shown good amounts of weight losses but with flatter tendency or smaller slope than the second stage. Overall, the total weight losses for LSC-6303NiCo, LSC-6306NiCo, and LSC-6309NiCo are 1.72%, 1.84%, and 2.22%, respectively. The weight loss values for LSC-6303NiCo, LSC-6306NiCo and LSC-6309NiCo have indicated that the amount of in-situ exsolved nanoparticles, as well as the number of oxygen vacancies, are increasing with an increased amount of doped catalytically active metals.

Figure 4.9 (b) shows the comparison of TGA curves for LSC-6309NiCo, LSC-6309Ni, and LSC-7309NiCo, and the weight losses for them are 2.22%, 2.27%, and 1.86%, respectively. All three curves have similar three stages of weight losses at 100°C to around 400°C, from 400°C to around 600°C, and from 600°C to 850°C. The starting and ending temperatures of each material are slightly different due to the different material compositions. LSC-6309NiCo had a similar weight loss with LSC-6309Ni, but LSC-6309NiCo has an obvious lower starting temperature and a larger amount of weight loss in stage two and the first half of stage three. Stage two and three are the main steps to introduce oxygen vacancies into the structure, where LSC-6309NiCo started at 380°C and 510°C, and LSC-6309Ni was at 420°C and 580°C. At the last part of stage three, at around 600°C the LSC-6309Ni has

increased its weight loss and resulted in a similar amount with LSC-6309NiCo. This result indicates that A-site deficient material, both from monometallic doping and bimetallic doping, shall have introduced a similar amount of oxygen vacancies into the structure, but bimetallic doped perovskite requires less energy for the exsolution process. LSC-7309NiCo has a smaller amount of weight loss than both LSC-6309NiCo and LSC-6309Ni, and the starting temperature for stage two and three are around 420°C and 580°C, which are higher than LSC-6309NiCo and can be concluded as the effects from the lack of A-site deficiency. By comparing the result of these TGA curves, It can be inferred that the formation of A-site deficiency and bimetallic doping of Ni & Co can facilitate the formation of oxygen vacancies into the structure, thereby improving ionic conductivity and catalytic activity.

4.2.4 SEM Result Analysis.

The previous discussion has revealed the effects of an A-site deficiency on perovskite exsolution, in that the existence of A-site deficiency in a perovskite can successfully facilitate the in-situ exsolution of metallic particles and the introduction of oxygen vacancies. Based on the XRD and TPR results, LSC-6309NiCo and LSC-6309Ni are inferred to have in-situ excluded a fair amount of metal particles. The identification process for the metal particles' exsolution is further analyzed by SEM microstructure images. The SEM images of the fresh LSC-6309NiCo and LSC-6309Ni are provided to compare with the reduced LSC-6309NiCo, and LSC-6309Ni samples. Both reduced samples have been pre-treated in 5% H_2–N_2 at 800 °C for 4 hours.

Figure 4.10 is the SEM image for microstructures of the fresh LSC-6309NiCo powder sample. Figure 4.11 (a) is the bulk image of reduced LSC-6309NiCo sample and Figure 4.11 (b) is a closer look on the exsolved nanoparticles with higher magnification. Clearly,

no exsolution of metallic nanoparticles could be found on the surface of the fresh sample. Compared with Figure 4.10, numerous amounts of exsolved nanoparticles are observed from Figure 4.11 (a) and (b). These exsolved particles are uniformly dispersed on the surface of the bulk with a diameter of around 50 nm to 70 nm, which conform to expectations. Figure 4.11 c) and d) are the point scanning results for reduced LSC-6309NiCo. The bulk phase in Figure 4.11 c) was marked as point (1), and the exsolved particle was marked as point (2). Figure 4.11 d) is the diagram showing the peaks for detected elements. In the diagram La is detected at 0.5, 4.7, 5.1 and 5.9 keV, Sr is at 1.8 keV and Cr is at 0.25 and 5.4 keV for both the bulk and exsolved particle. Moreover, distinct Co and Ni peaks are detected at point (2) at 7 and 7.5 keV respectively, while the peaks for point (1) are weak at these positions. This result has verified the exsolution particles from LSC-6309NiCo to the surface of the LSC base under reduction are indeed Ni-Co alloy.
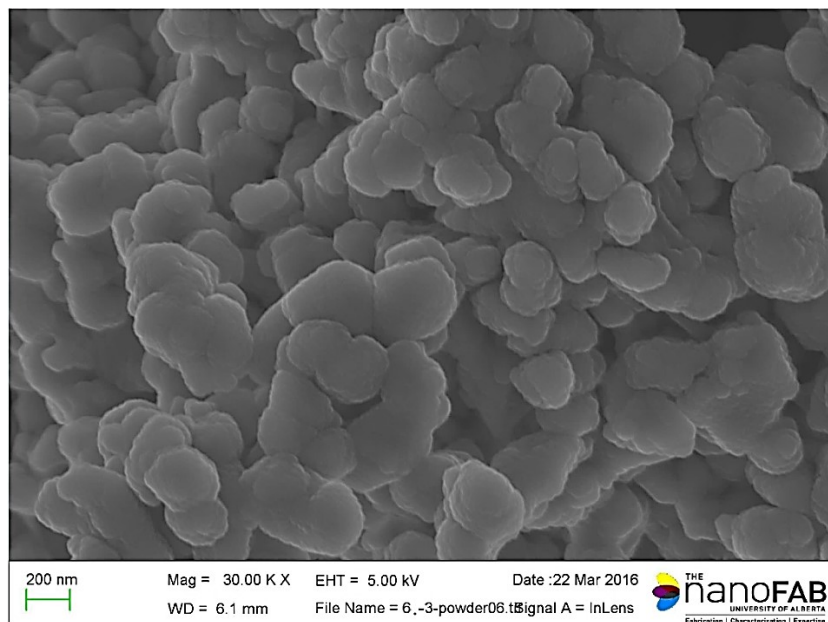
Figure 4.10. SEM image for fresh LSC-6309NiCo microstructure.
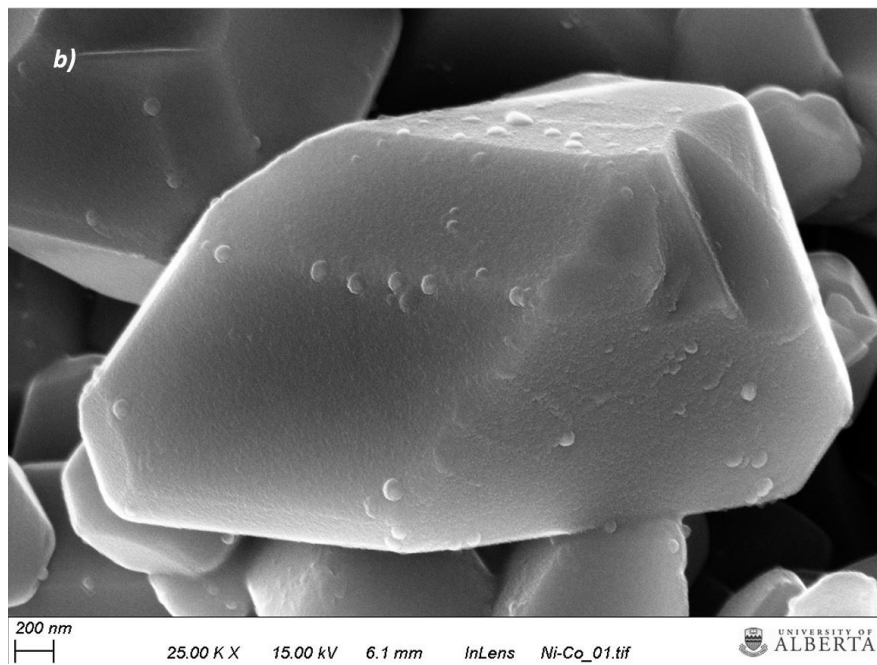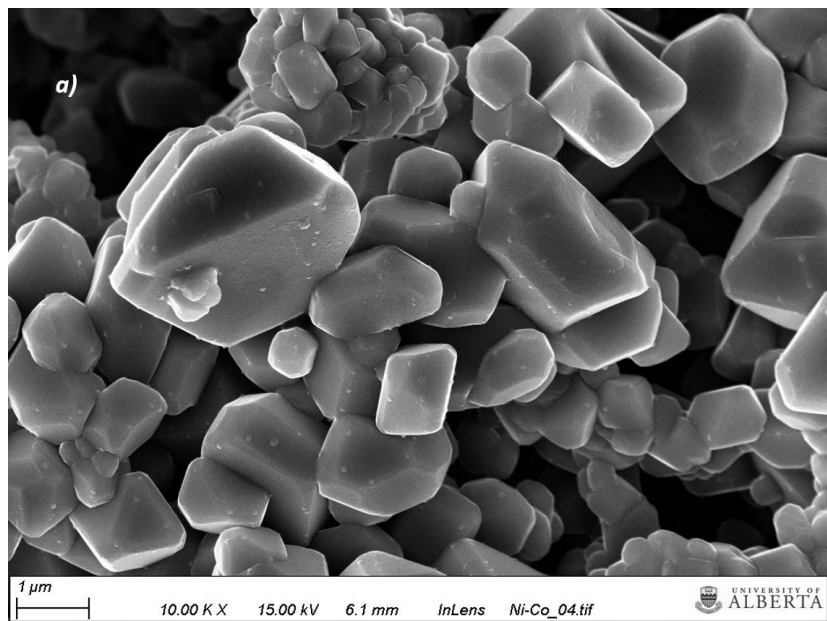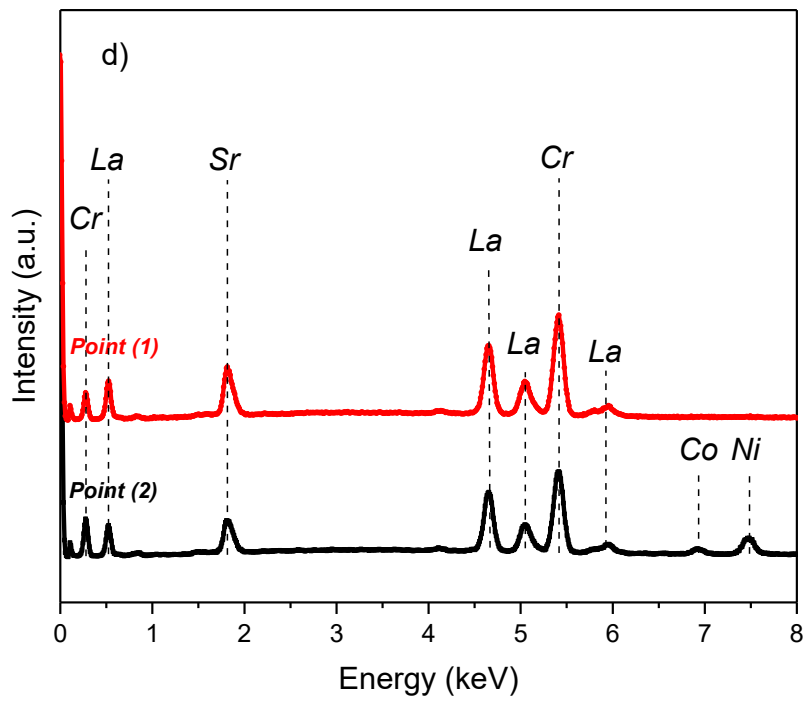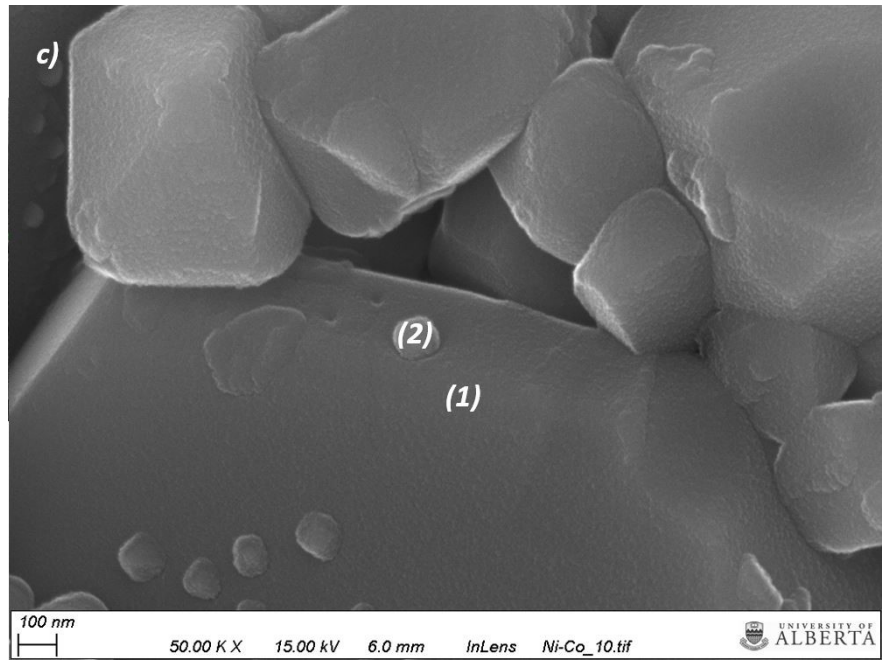
Figure 4.11. SEM images for reduced LSC-6309NiCo microstructures a) the bulk b) the bulk with higher magnification c) & d) are the SEM image and correlated point scanning results.

Figure 4.12 shows the SEM image for fresh LSC-6309Ni powder sample's microstructure. As for the fresh LSC-6309NiCo's SEM image, no clear exsolved nanoparticles are found on the fresh LSC-6309Ni sample's surface. In contract, reduced LSC-6309Ni has shown a large amount of exsolved nanoparticles in Figure 4.13 a) & b). These exsolved nanoparticles are well decorated on the surface of the bulk material with a diameter of 50 nm to 70 nm, which is similar to the size of exsolved Ni-Co alloy shown in Figure 4.11. Figure 4.13 c) & d) are the SEM image with its correlated point scanning results. The bulk base in Figure 4.13 c) was selected as point (1) and one exsolved particle in the figure was marked as point (2). The detected elements for points (1) and (2) are expressed by Figure 4.13 (d). The La element is detected at 0.5, 4.7, 5.1 and 5.9 keV, Sr is at 1.8 keV and Cr is at 0.25 and 5.4 keV for both points (1) and (2) for LSC-6309Ni, which are at exactly the same positions as the LSC-6309NiCo. A small peak of Ni element is detected at 0.8 keV for point (1), which might indicate the existence of Ni in the bulk. Strong peaks of Ni element are detected at both 0.8 and 7.5 keV that indicates the formation of exsolved Ni particles.

100 nm | Mag = 50.00 K X | EHT = 5.00 kV | Date :22 Mar 2016 | nanoFAB
| WD = 6.1 mm | File Name = 6.-3-powder01.tif | Signal A = InLens | THE nanoFAB UNIVERSITY OF ALBERTA Fabrication | Characterization | Expertise
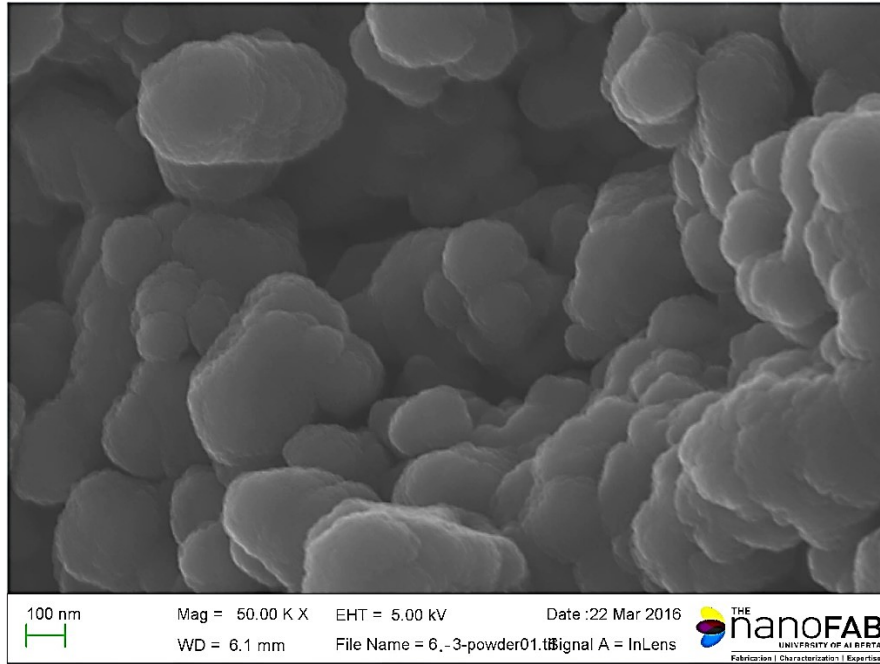
Figure 4.12. SEM image of fresh LSC-6309Ni microstructure.

a)

1 μm | 15.00 K X | 15.00 kV | 5.6 mm | InLens | Ni_04.tif | UNIVERSITY OF ALBERTA
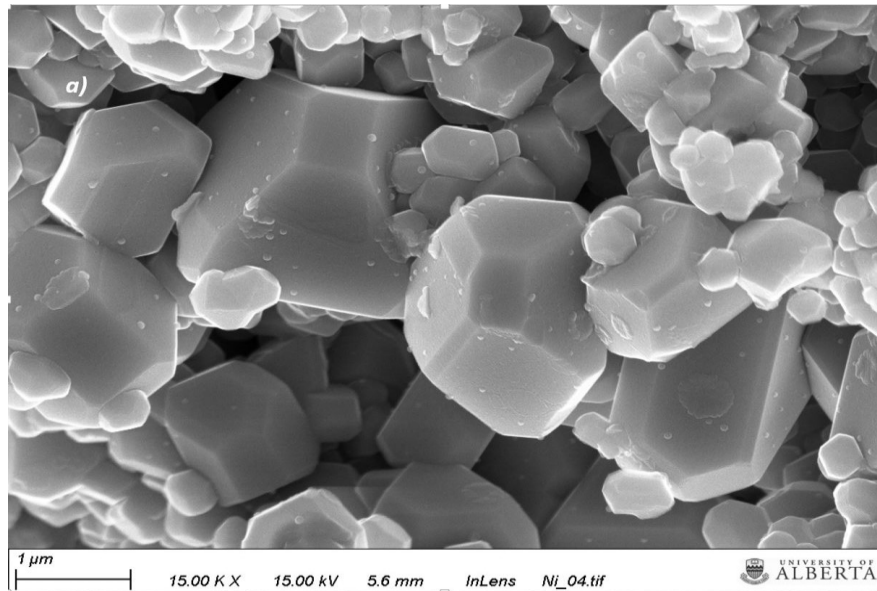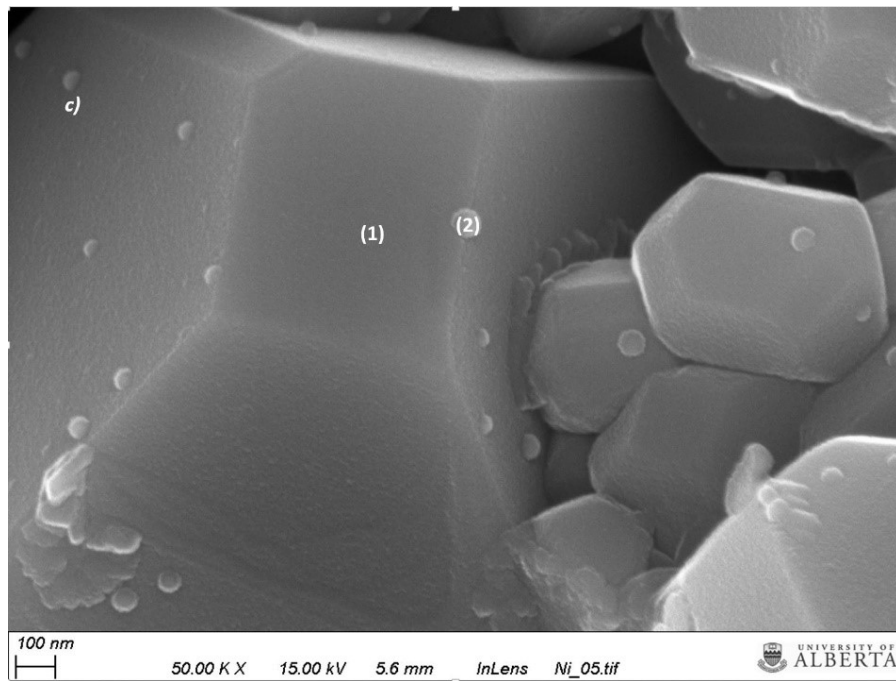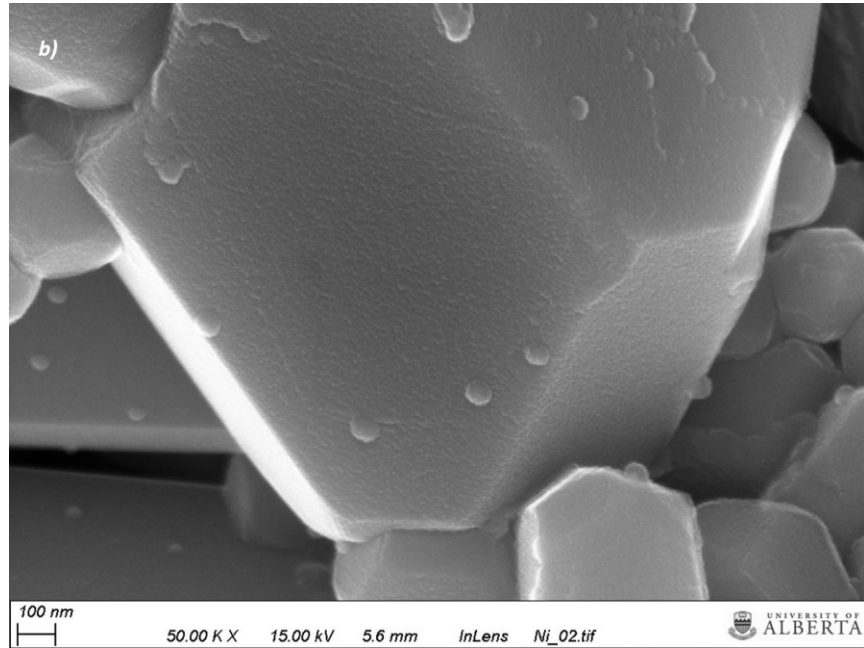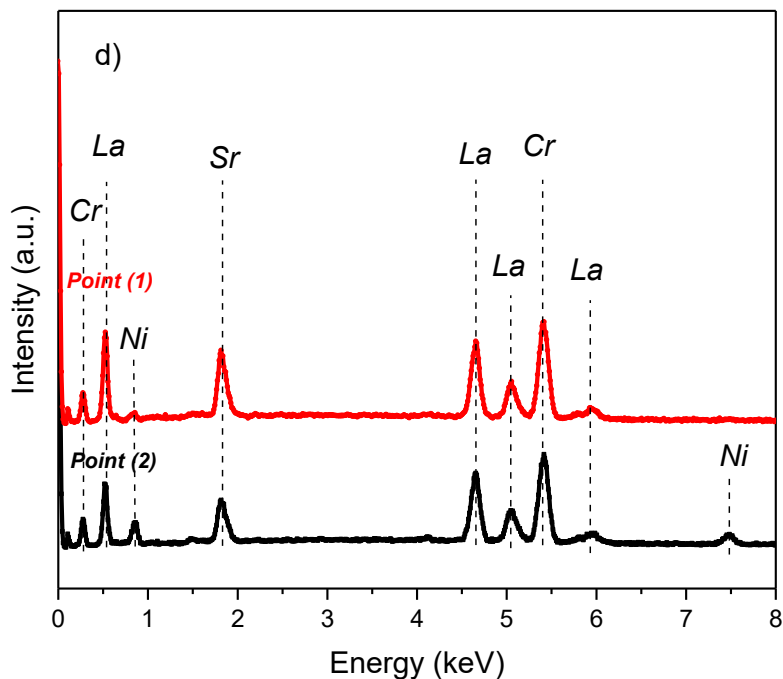
Figure 4.13. SEM images for reduced LSC-6309Ni microstructures a) the bulk b) the bulk with higher magnification c) & d) are the SEM image and correlated point scanning results.

4.3 Electrochemical Performances of the Cell

Previous studies have concluded the importance of in-situ exsolution for electrochemical performance. In-situ exsolution of metal nanoparticles, especially Ni particles has led to high electronic conductivity and high catalytic activity, which successfully promotes the electrochemical performance.[58,36] Both LSC-6309NiCo and LSC-6309Ni have demonstrated the largest amount of exsolution from XRD, TPR and TGA results. Therefore, the LSC-6309NiCo has been applied as an anode material in SOFC, with the electrochemical performance measured in both H_2 and syngas environment. For comparison, the performance of LSC-6309Ni was also measured, in order to identify the

functional effects of bimetallic doping and monometallic doping for electrochemical performances. For further investigation, the fabricated material was also applied as a cathode electrode for CO_2 reduction in a solid oxide electrolysis cell (SOEC), which is the reverse mode of SOFC.

The SEM image of the cross-section microstructure for the tested cell is shown in Figure 4.14. As revealed by the figure, the dense YSZ was placed in the middle as the electrolyte with a thickness of 300 μm, and the LSCF perovskite oxide was used as the air electrode for all the tested cells. Two 15 μm GDC buffer layers were introduced between the electrode and the electrolyte. The approximately 30μm fuel and air electrode layers were applied above the GDC layers. The current collector layers by Au paste were painted on the electrodes.
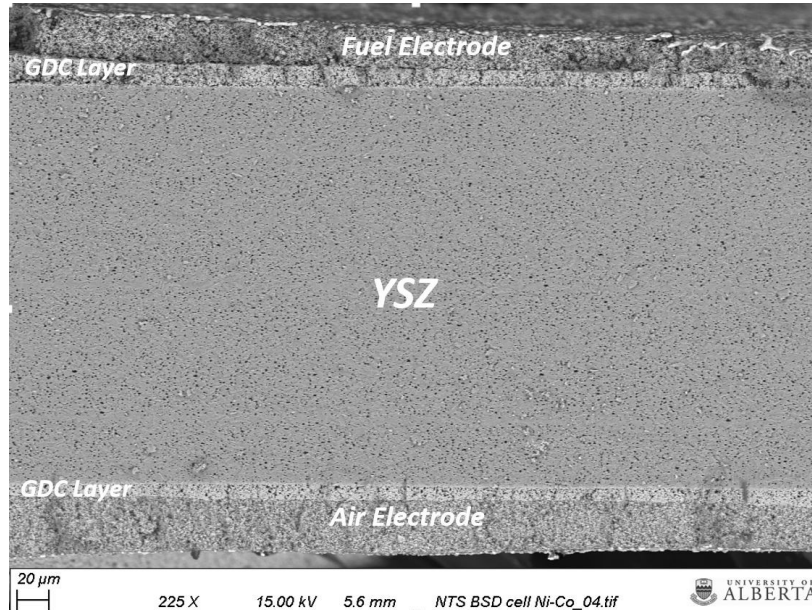
Figure 4.14. SEM image of the cross-section area of the cell.

4.3.1 Electrochemical Performance: j-V Curves.

4.3.1.1 j-V Curves for Anode Functional Test in Pure H₂ and Syngas.

Figure 4.15 is the j-V curve for LSC-6309NiCo and LSC-6309Ni (anode) cells at 850°C in pure H_2 gas. The tested cells were reduced with 5% H_2/N_2 gas for two hours before testing. In H_2 gas, the OCV values for LSC-6309NiCo and LSC-6309Ni cells were similar, which were 1.15V and 1.13V respectively. The high values of OCV observed indicated no gas leakage was present in the electrolyte. Figure 4.15, the j-V diagram has revealed the maximum power produced by LSC-6309NiCo cell as 329 mW/cm^2 with a current density of 599 mA/cm^2, while the LSC-6309Ni cell has a maximum power output of 237 mW/cm^2 with a current density of 441 mA/cm^2. This result denotes that the bimetallic doping of Ni-Co alloy to the LSC base can significantly improve electrochemical performance for monometallic Ni doped LSC for H_2 oxidation reactions.
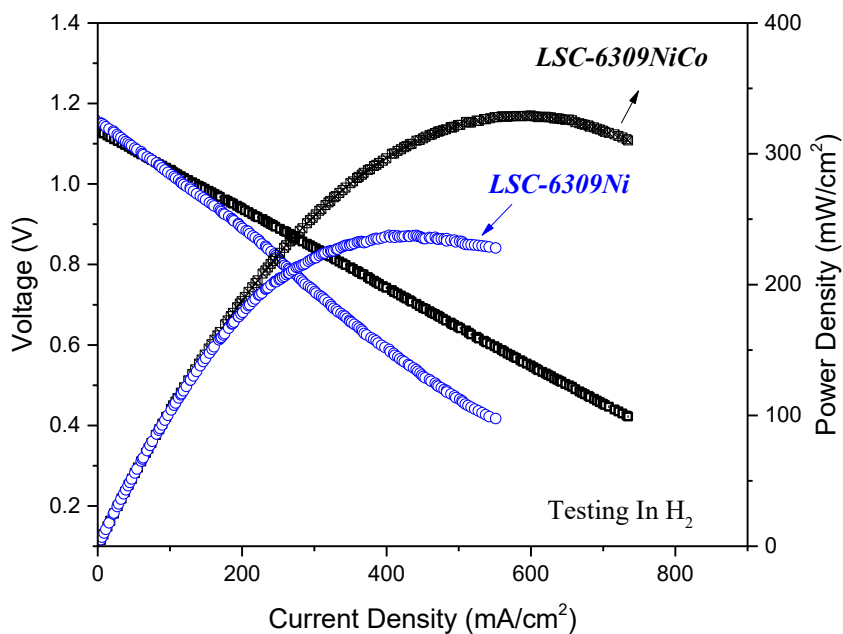
Figure 4.15. j-V curves of LSC-6309NiCo and LSC-6309Ni at 850°C in pure H₂ gas.

A possible reason for promoting electrochemical performance of the bimetallic doped cell in pure H_2 might be the synergistic reactions of the Ni-Co alloy. Ding et. al[61] have studied the different electrical properties of Ni-Co alloy and Ni and Co doped LSC cells, and concluded that Ni-Co alloy doped cell has shown the highest electronic conductivity compared to others. The higher electronic conductivity of Ni-Co alloy doped cell can be postulated as due to the interactions between Ni and Co ions that provide more electron holes into the system.[61] Moreover, the SEM images of LSC-6309NiCo and LSC-6309Ni from Figure 4.11a) and Figure 4.12 a) have shown a larger amount of exsolved nanoparticles of Ni-Co alloy than Ni, which brings an increased number of TPBs and active sites to the cell that promotes the overall performance. In addition, Ni-Co alloy has been investigated to have a larger pre-exponential term in the Arrhenius equation (Equation 19) than Ni at 800 °C that may suggest a higher electrochemical reaction rate of the Ni-Co cell than the Ni doped cell for electrochemical conversions.[62]

$$k = Ae^{-E_a/(RT)} \quad (19)$$

The electrochemical performance for LSC-6309NiCo and LSC-6309Ni cells in syngas with 60% CO and 40% H_2 were examined, and the electrochemical performance results were plotted. Theoretically, the OCV values and power densities observed in syngas should be closer to these values in pure H_2 gas with the higher the amount of H_2 in syngas, at the same operating temperature.[63]

Figure 4.16 illustrates the electrochemical performance diagram for LSC-6309NiCo and LSC-6309Ni cells in syngas at 850°C. The OCV values of 1.11V and 1.14V are determined as expected for LSC-6309NiCo and LSC-6309Ni, respectively, in syngas. LSC-6309NiCo cell has produced about 258 mW/cm^2 as the maximum power density and 455mA/cm^2 as the current density in syngas while the LSC-6309Ni cell has a maximum power density of

170 mW/cm^2 and with current density of 307mA/cm^2. These results demonstrate that the Ni-Co alloy doped LSC cell has maintained the promoted catalytic activity for syngas oxidation. However, the maximum output of power density in syngas is still lower than the maximum power density in H$_2$ gas for both cells. This can be explained by the smaller amount of H$_2$ contained in syngas compared to the pure H$_2$ gas, and the cells might have weaker catalytic activity for the oxidation of CO that pulls down the overall amount of power output.
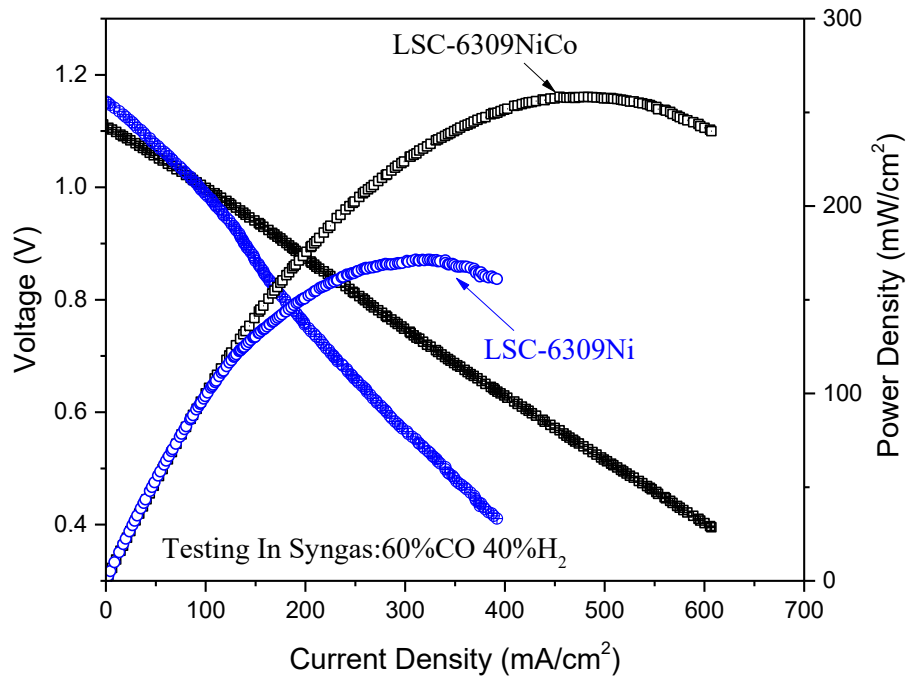
Figure 4.16. j-V curves of LSC-6309NiCo and LSC-6309Ni at 850°C in syngas.

4.3.1.2 j-V Curves for Cathode Functional Test in CO&CO$_2$

First of all, the structure's stability of the LSC-6309NiCo and LSC-6309Ni fuel electrodes in CO$_2$ gas were characterized by XRD. Both samples were treated in CO$_2$ gas at 850°C

for 24 hours. The XRD results are shown in the Figure 4.17. Both LSC-6309NiCo and LSC-6309Ni have maintained the perovskite oxide phase of LSC after treatment, which indicates that the base structures of both materials have not been destroyed in the CO_2 atmosphere. However, the diffraction peaks of NiO have been found in both materials as detected peaks at 37°, 43° and 63° in the XRD diagram as marked by stars (*). The existence of the NiO phase proves the exsolved Ni particles and Ni-Co alloy has been oxidized to NiO by CO_2 gas.
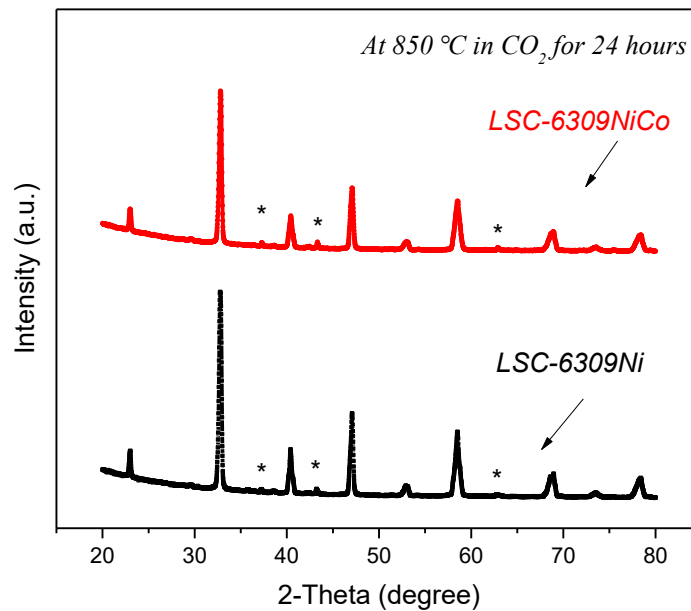
Figure 4.17. XRD diagram of LSC-6309NiCo and LSC-6309Ni in CO_2 for 24 hours.

The electrochemical performances of SOEC using LSC-6309NiCo and LSC-6309Ni cathodes were processed at 850 °C in the CO_2/CO atmosphere at the ratio of 70:30. CO gas was added into fuel gas CO_2 during the electrochemical test to prevent the oxidation of exsolved particles. The cells were tested mainly under electrolysis mode (negative current density) with applied voltages from 0V to 0.9V (vs. OCV).

Figure 4.18 has illustrated the j-V curve of the cathode functioned LSC-6309Ni and LSC-6309NiCo cell. In Figure 4.18, the open circuit potential for both cells are around 0.84V to 0.82V, which is close to the theoretical values for the CO&CO_2 atmosphere. As depicted, the LSC-6309NiCo cell has current densities of 0.039 mA/cm^2, 0.136mA/cm^2, 0.245mA/cm^2, and 0.41mA/cm^2 at applied voltages of 0.1V, 0.3V, 0.5V and 0.7V, respectively, while LSC-6309Ni has corresponding current densities of 0.027mA/cm^2, 0.089 mA/cm^2, 0.179 mA/cm^2 and 0.286 mA/cm^2. The LSC-6309NiCo cell has expressed better performance than the LSC-6309Ni cell in 70%CO_2 & 30% CO at all applied voltages, which demonstrates that the bimetal doped LSC cell has a better catalytic property in the CO_2 reduction process. The current density for the LSC-6309NiCo cell stops growing when the voltage applied goes higher than 1.61V, and the current density stops at 1.65V for the LSC-6309Ni cell.
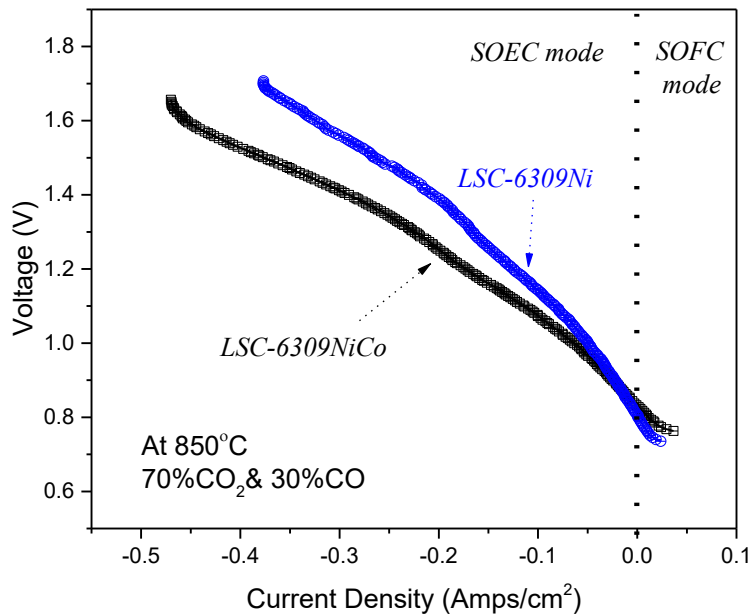
Figure 4.18. j-V curves of LSC-6309NiCo and LSC-6309Ni at 850°C in CO&CO_2.

This result demonstrates that both cells may occur large values of resistance at higher applied voltage that may degrade the cells; thus the optimum applied voltage for metallic doping LSC SOEC shall be lower than 0.75V vs. OCV.

4.3.2 Electrochemical Performance: EIS Curves.

Generally, the ohmic electrolyte resistance and the electrode polarization resistance mainly contribute to the voltage loss appearing during fuel cell operation (j-V curves). Thereby, to create a clear comparison and better understanding of the electrochemical performance of the tested cells, their correlated EIS diagrams were also measured in pure H_2 gas, syngas, and CO&CO_2 environment.

4.3.2.1 EIS Results for Anode Functional Test in pure H_2 and Syngas.

Figure 4.19 illustrates the EIS performance of both LSC-6309NiCo and LSC-6309Ni cells from 10^6 Hz to 0.1 Hz under open circuit voltage condition with H_2 gas at 850°C. The curves intersections with the real axis (x-axis) at high frequencies represent their ohmic resistance, which is mainly caused by the electrolyte material.[64] LSC-6309NiCo and LSC-6309Ni cells have shown an ohmic resistance of 0.54 Ω and 0.56 Ω, which are reasonable with the 300 μm thickness of the YSZ electrolyte. The difference between the two intersections at high frequency and low frequency with the x-axis represents the activation polarization resistance, which is the sum of the electrode (anode and cathode) reaction resistances.[65] The real part of the impedance at low frequency for LSC-6309NiCo and LSC-6309Ni are partially compared at 10Hz, 1Hz, and 0.1Hz as marked by the dashed lines in the figure. LSC-6309NiCo cell has shown a clear reduction of the real impedance compared to LSC-6309Ni at the identical frequencies. This result has demonstrated the lower polarization resistance of LSC-6309NiCo cell compared with the LSC-6309Ni cell. The

lower value of polarization resistance for the LSC-6309NiCo also clarifies its superior electrochemical performance with a higher value of power generation in H_2 gas, which is consistent with the j-V curve in Figure 4.15.
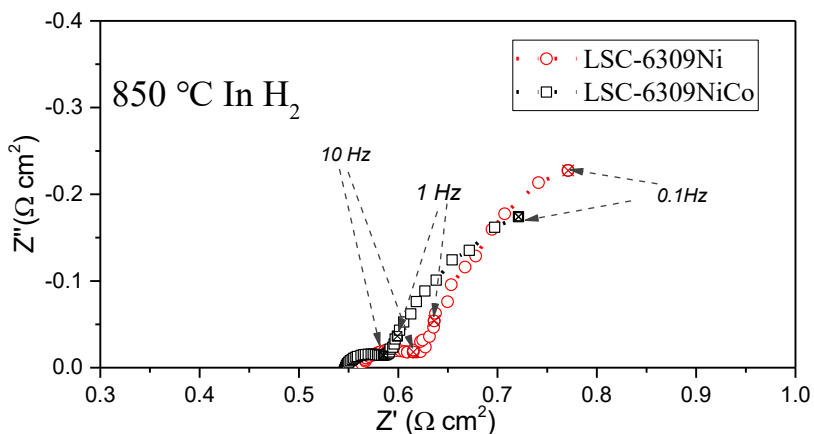
Figure 4.19. EIS curves of LSC-6309NiCo and LSC-6309Ni at 850°C in pure H_2 gas.

Figure 4.20 is the EIS diagram for LSC-6309NiCo and LSC-6309Ni cells for syngas oxidation at 850°C in OCV condition. Compared with the H_2 oxidation EIS diagram in Figure 4.19, no significant increase of ohmic resistances are found in syngas atmosphere. In addition, the real impedance values of each cell are compared at 10Hz, 1Hz and 0.1Hz. Apparently, LSC-6309Ni has an obvious larger value of real impedance than LSC-6309NiCo under each frequency. So, as consistent with the j-V curve in Figure 4.16, a larger polarization resistance of LSC-6309Ni in syngas can be concluded. This may indicate that negative effects from CO (coal syngas) might be stronger with the Ni particles than the Ni-Co alloy in a LSC cell that creates higher activation polarization for the cell.
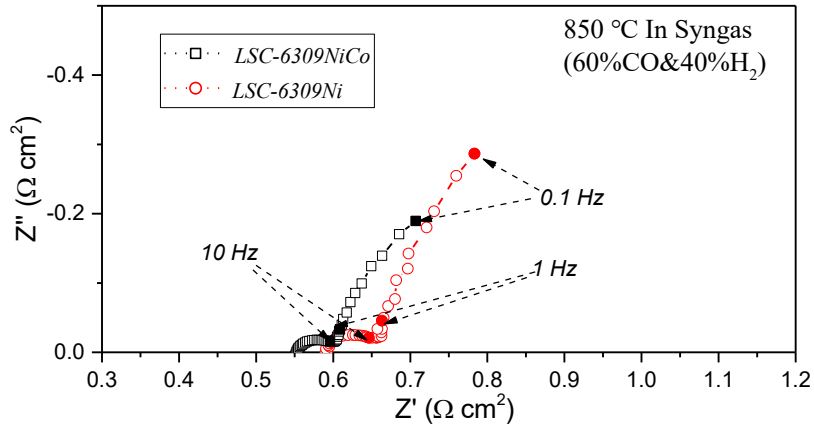
Figure 4.20. EIS curves of LSC-6309NiCo and LSC-6309Ni at 850°C in syngas.

4.3.2.2 EIS Results of Cathode Functional Test in CO&CO₂.

The EIS performances for the LSC-6309NiCo and LSC-6309Ni cells in 70% CO_2 & 30%CO at 850°C were analyzed and plotted. Figure 4.21 shows the EIS performance from 10^6 Hz to 0.1Hz of the LSC-6309NiCo and LSC-6309Ni cells in SOEC mode at OCV. Both cells have similar ohmic resistance as they should in SOFC mode; however, both of them have shown distinctly higher polarization resistance in SOEC mode than in SOFC mode, which indicated the lower catalytic activity for CO_2 reduction than H_2 & syngas oxidation of both cells. In addition, the real value of impedance for both cells have been specifically compared at 0.1Hz, 1Hz and 10Hz, and the LSC-6390NiCo cell has given smaller resistance than the LSC-6309Ni cell at all tested frequencies. Therefore, even though both LSC-6309NiCo and LSC-6309Ni cells' catalytic activities become lower in CO_2 gas for SOEC tests, the exsolution of Ni-Co alloy still has better catalytic performance than Ni particles in a CO_2 atmosphere.
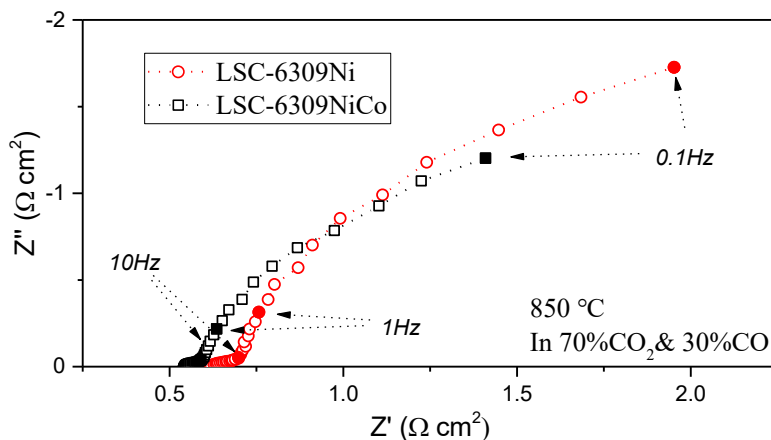
Figure 4.21. The EIS curves of LSC-6309NiCo and LSC-6309Ni at 850 °C in CO&CO₂.

The EIS performances for the LSC-6309NiCo and LSC-6309Ni cells under different applied voltages in CO_2&CO at 850°C were measured and plotted in Figure 4.22 as well, where a) is for LSC-6309NiCo cell and b) is for LSC-6309Ni cell. Different voltages of 0V, 0.1V, 0.3V, 0.5V, 0.7V and 0.9V vs. OCV are applied on both cells. The ohmic resistances for both cells are similar under all tested voltages. The polarization resistances were compared at the real value of impedance at 0.1Hz for each curve. The polarization resistances for both cells are clearly decreased with increased applied voltage from OCV to 0.1V vs. OCV to 0.3V vs. OCV. The polarization resistances of the cells are similar at 0.3V, 0.5V and 0.7V (vs. OCV). When the applied voltages have reached 0.9V, the polarization resistances for both cells have been abruptly increased to a large value. The high resistance that occurs at 0.9V vs. OCV confirmed the electrochemical performance in their j-V curve in Figure 4.18 that showed the optimum applied voltages for both cells are suggested to be lower than 0.75V vs. OCV. The decreased polarization resistance with increased applied voltage implies the successful activation of the electrode from the external voltage that remarkably improves the cell's performance.[66] The increasing polarization resistance from 0.7V to 0.9V vs. OCV for both cells might be attributed to

diffusion limitations. The cell produces a higher amount of product gas with higher applied voltage; however, if the diffusion rate of produced gas is not high enough, then the reaction rate will be limited by the mass transfer rate and, therefore, deactivate the cell.
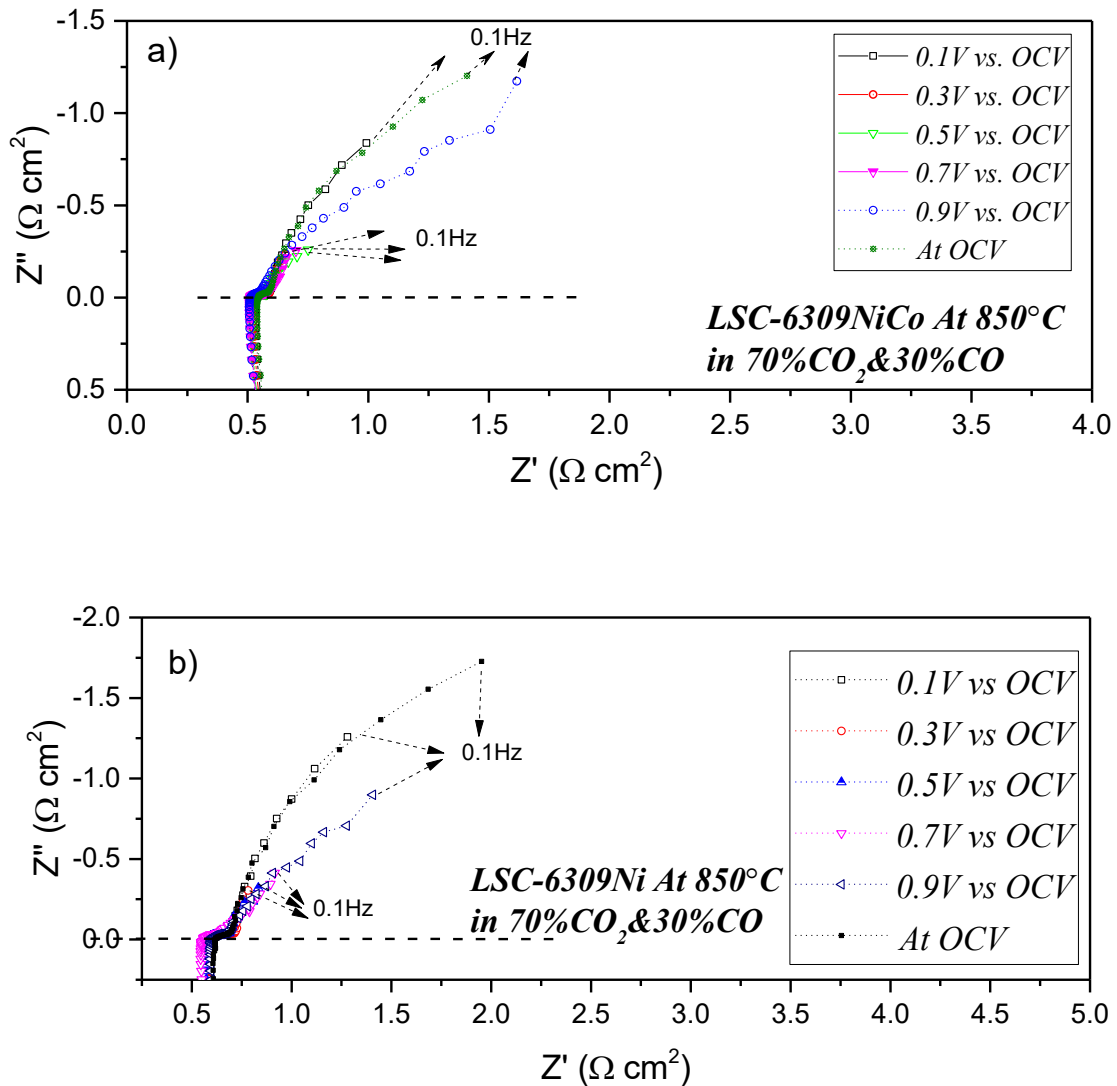
Figure 4.22. Experimental SOEC EISs at different applied voltages in the atmosphere of CO2/CO (70:30) (a) for LSC-6309NiCo (b) for LSC-6309Ni.

4.3.3 Electrochemical Performance: Stability Tests

4.3.3.1 Stability Test in SOFC Operations

The LSC-6309NiCo cell was selected for the stability test based on its good electrochemical performance in previous tests. Figure 4.23 is the 30-hour stability test curve of LSC-6309NiCo cell in H_2 with a constant voltage of 0.85V. The cell has illustrated superb stability as expected. With 0.85V working voltage, about 290 mA/cm^2 current density has been continuously recorded from the beginning to the end, and no cell degradation has been found. The value of current density recorded in the stability test fits the correlated voltage and current density values in the j-V curve in Figure 4.15. Therefore, the good cell performance of LSC-6309NiCo has been perfectly maintained during the entire 30 hours of operation; the excellent stability of the cell can be concluded.
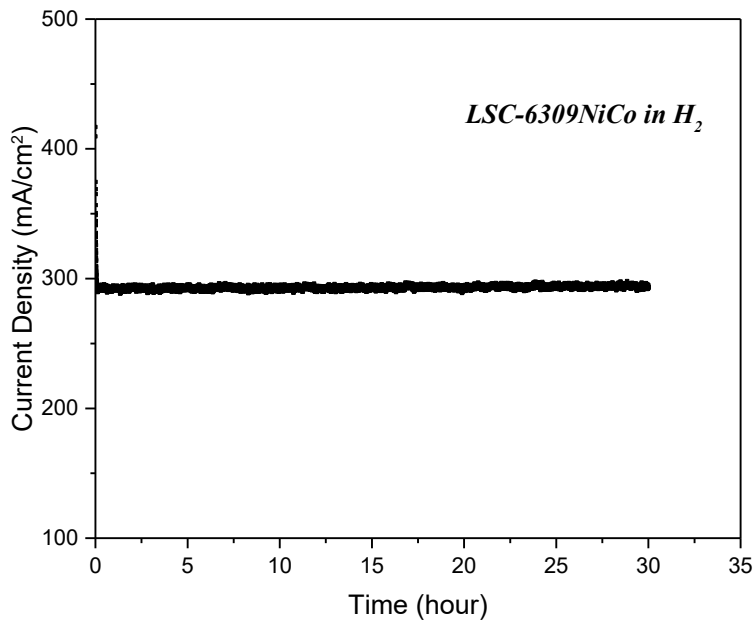
Figure 4.23. The 30 hours' stability test for LSC-6309NiCo in H_2 at constant 0.85V voltage.

The LSC-6309NiCo cell was tested for the stability in syngas as well. Figure 4.24 is the 30 hours' stability test curve of LSC-6309NiCo cell in syngas with a constant voltage of 0.83V. The cell has shown excellent stability in syngas as in H_2 gas. A constant current density of 220 mA/cm^2 was maintained during the whole test in the graph under the 0.83V working voltage. These values correlate with the j-V curve in Figure 4.16, and no obvious cell degradation was found. Therefore, LSC-6309NiCo cell has perfectly exhibited its excellent stability in both hydrogen and syngas.
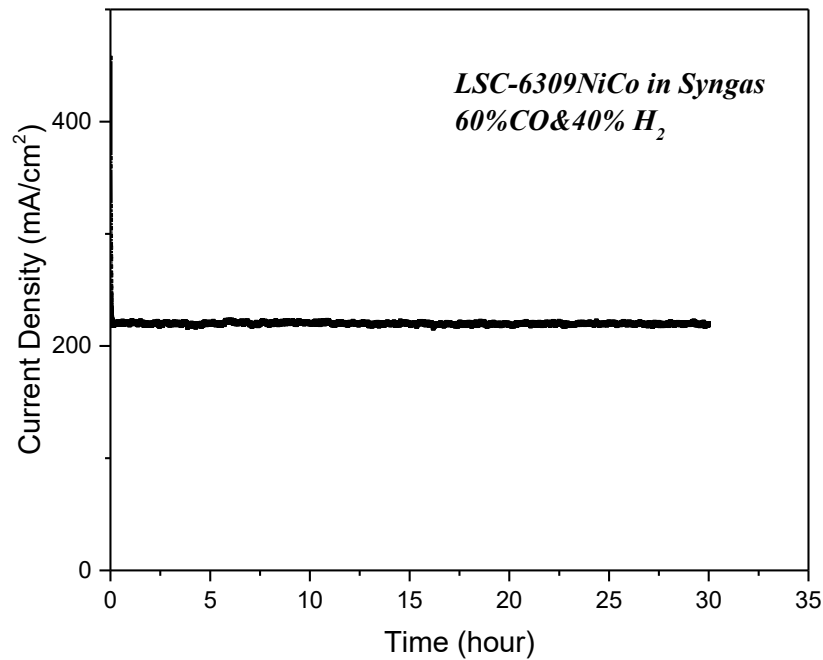
Figure 4.24. The 30-hour stability test for LSC-6309NiCo in Syngas at a constant voltage of 0.83V.

4.3.3.2 Stability Test in SOEC Operations

Short term operating stabilities for LSC-6309NiCo and LSC-6309Ni electrolysis cells were tested in 70% CO_2 & 30% CO at 850°C with various applied voltages and plotted in Figure 4.25, where a) is for the LSC-6309NiCo cell and b) is for the LSC-6309Ni cell. Both cells were run in the SOEC mode for 30 minutes at constant voltages of 0.1V, 0.3V and 0.5V (vs. OCV). The LSC-6309NiCo electrolysis cell has shown good stabilities under all voltages and the current densities of the cell increase with increasing applied voltage. In contrast, the LSC-6309Ni electrolysis cell has expressed good stabilities at applied voltages of 0.1V and 0.3V. A significant degradation of the LSC-6309Ni cell was detected at 0.5V applied voltage in Figure 4.25 b) such that the current density at 0.5V applied voltage on the LSC-6309Ni cell is very close to its current density at 0.3V vs. OCV. The possible reason for this degradation might be the influence from carbon deposition on Ni particles from the over reduction of the CO & CO_2 gas.[67] As the result, the stable operating potential for LSC-6309Ni can be inferred as 0.3V vs. OCV. Overall, the bimetallic doped LSC perovskite has shown better stability than the Ni doped LSC in an SOEC atmosphere with various applied potentials.
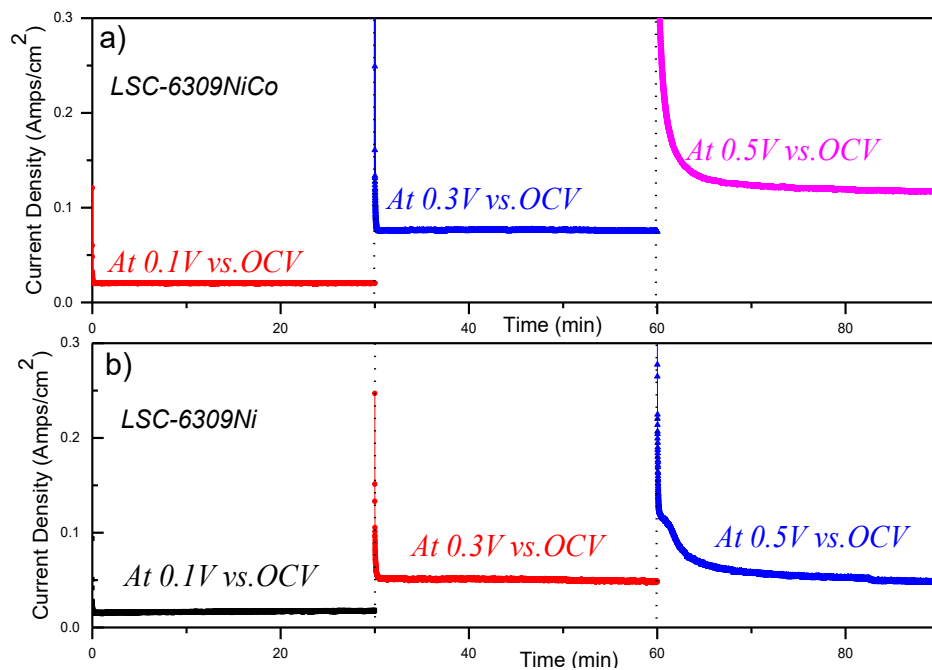
Figure 4.25. Short term stabilities of the electrolysis cells with (a) LSC-6309NiCo and (b) LSC-6309Ni cathodes at 850 °C at various applied voltages.

Figure 4.26 shows a plot of the long-term stability test for LSC-6309NiCo electrolysis in 70% CO_2 & 30% CO at 850°C with 0.3V applied voltage for around 48 hours. The current density of the cell has experienced a slight decrease in the first five hours and then remained stable for the entire duration of the test. This 48-hour durability test suggests that there is no evident degradation of the LSC-6309NiCo based cell during the electrolysis of CO_2.
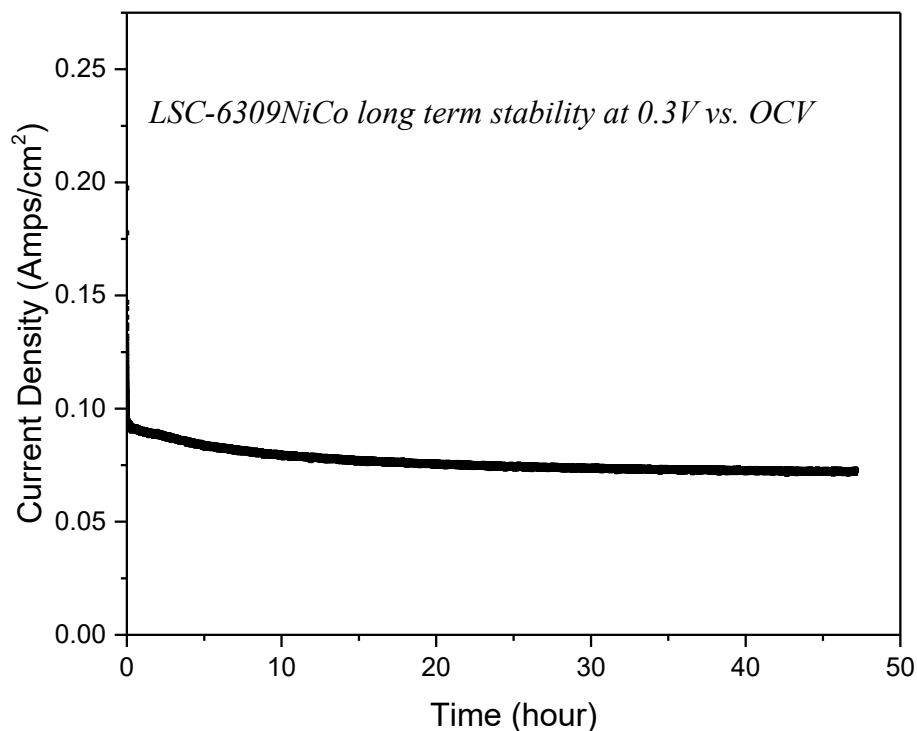
Figure 4.26. Stability test of LSC-6309NiCo electrolysis cell at 0.3V vs. OCV.

4.4 Carbon Deposition Analysis.

Previous studies have indicated the poor carbon deposition resistance of Ni particle doped fuel electrodes operating in coal gases. The coal derived fuel gas applied to solid oxide cells such as hydrocarbons, syngas, and even CO_2 gas can cause carbon deposition and lead to serious degradation to the cell.[22,63,67,68] Therefore, carbon deposition resistance is also another important parameter for catalytic activity analysis of the electrode. The carbon deposition resistance of Ni and Ni-Co LSC perovskite oxide was studied in this research by O_2-TPO analysis. TPO is the temperature programmed oxidation analysis that uses the measurement from TGA and MS to analyze the material's oxidation process. First of all,

the powders of electrode LSC-6309NiCo and LSC-6309Ni were placed into the MTI GSL-1100X tube furnace to be sintered with CH_4 gas at 850°C for 24 hours. After the treatment with CH_4 gas, the samples were inserted for the TGA test from 0°C to 850°C in air. The gas outlet of the TGA was connected with the MS; therefore, the specific amount of produced CO_2 at different temperatures could be measured. The O_2-TPO profile measured by MS is shown in Figure 4.27.
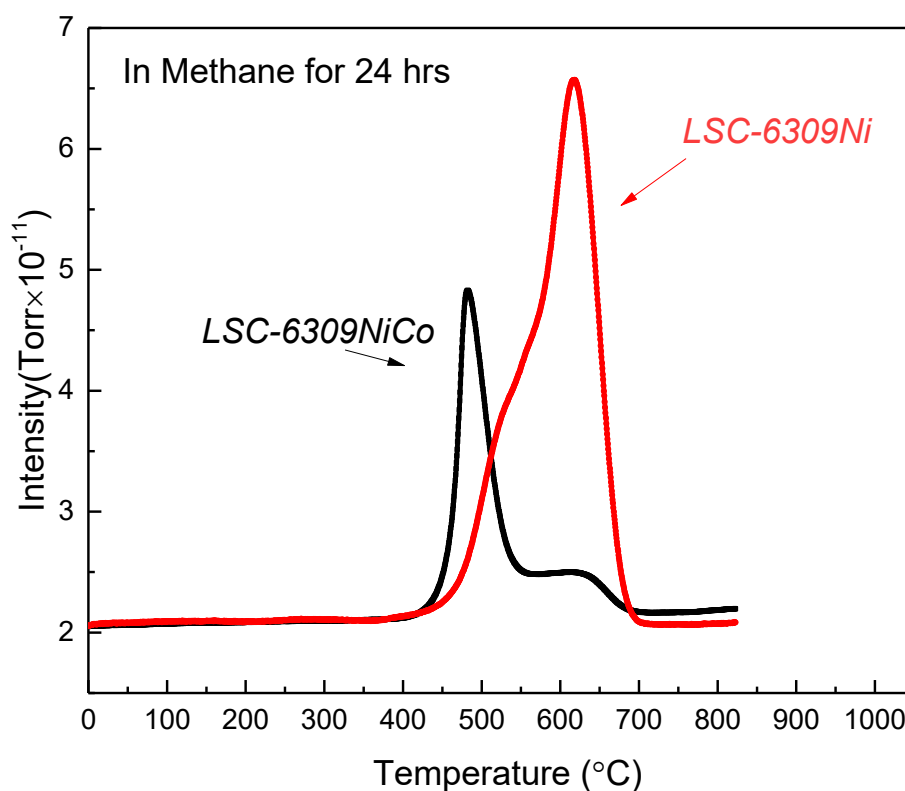
Figure 4.27. TPO curves for CH4 treated LSC-6309NiCo and LSC-6309Ni.

The CO_2 peak areas for LSC-6309NiCo and LSC-6309Ni were 4.21×10^{-9} and 5.30×10^{-9} respectively. From this result, it can be concluded that compared with Ni doped catalytic material, the addition of Co into the catalyst can effectively suppress the formation of

carbon deposition on the electrode material as studied by K.Takanabe et al.[40] Moreover, it can also be found, by comparing the peak position of the CO_2 curves, that the peak position of LSC-6309Ni electrode material is at around 620°C while the peak position for the LSC-6309NiCo curve is around 470°C. The lower temperature for LSC-6309NiCo material indicates a smaller energy required for redox treatment. The higher carbon deposition resistance and lower required recovery temperature of LSC-6309NiCo than LSC-6309Ni can be explained by the bimetallic Ni-Co alloy analysis from previous studies, which indicates that the formation of surface Ni-Co alloy can effectively suppress the bonding of undesired carbon and preferentially oxidize the carbon atom into gas phase. The monometallic Ni is more likely to facilitate the formation of carbon-carbon bonds.[39,69]

Chapter 5 Conclusions and Future Work

5.1 Conclusions

The LSC-based perovskite oxides were studied in this research as a potential electrode material for SOFC and SOEC. A-site stoichiometric and A-site deficient LSC perovskite oxides were fabricated with monometallic Ni doping and bimetallic Ni-Co alloy doped into B-sites. The characterization of the material's fabrication and exsolution process were measured by XRD, TPR, TPO, TGA and SEM. LSC-6309NiCo and LSC-6309Ni were selected for the electrochemical performance tests in SOFC and SOEC due to their highest amount of nanoparticle exsolution. The following conclusions can be drawn based on the experimental results:

- The single-phase B-site Ni and Co doped LSC perovskite oxide can be successfully fabricated by the sol-gel combustion method with the doping proportion of 9 mol %.

- The existence of A-site deficiency can be regarded as the key to drive the exsolution of reducible B-site nanoparticles. Nano scaled Ni particles and Ni-Co alloy particles were exsolved from the perovskite oxides with uniform distribution.

- The exsolution process of Ni-Co alloy was found to be easier than Ni particles under a reducing atmosphere, indicating that the Ni-Co alloy exsolution required a lower temperature than Ni particles for a similar amount of exsolution.

- The doping of Ni in A-site deficient LSC has shown good the catalytic activity, and the Ni and Co alloy doped A-LSC materials express even better electrochemical performance in terms of lower polarization resistance and higher current density at the same operation voltage with pure H_2, 60% CO and 40% H_2 syngas as the fuel in SOFC and in a CO and CO_2 atmosphere in the SOEC mode, which could be

ascribed to the synergetic effects formed at the catalytically active Ni-Co alloy surface.

- A LSC-6309NiCo cell can be considered as a potentially cost-effective SOFC anode material for long-term operation that has perfectly maintained the excellent operating stabilities in various fuel gases, such as H_2 gas, syngas, and CO_2 and CO gas. Meanwhile, the formation of Ni-Co alloy has efficiently reduced the carbon deposition in the cell; therefore, performance degradation has been prevented.

5.2 Future Work

It is noted that the bimetallic Ni and Co doped into A-site deficient LSC perovskite oxide has performed shown enhanced electrochemical performance as the anode electrode in SOFC with H_2 gas and syngas as the fuel. To further improve its cathode performance in SOEC as well as the catalytic activity to other gases without losing its great stability and carbon deposition resistance, the doping ratio of Sr at A-sites and/or increase the A-site deficient ratio are suggested as reasonable pathways of investigation for the future, which is expected to bring higher conductivity to the bulk material and enhance the amount of exsolved nanoparticles on the surface. In addition, more experiments about the microstructures and the characterization of exsolved Ni-Co alloy particles with different Ni and Co ratios can be conducted to investigate the synergistic effects of the Ni-Co alloy in the future.

References:

(1)   Pérez-Lombard, L.; Ortiz, J.; Pout, C. A Review on Buildings Energy Consumption Information. *Energy Build.* **2008**, *40* (3), 394–398.

(2)   Iea. Key World Energy Statistics 2009. *Statistics (Ber).* **2009**, 82.

(3)   Electricity Generation using Steam Turbines http://www.mpoweruk.com/steam_turbines.htm.

(4)   Sims, R. E. H.; Rogner, H.-H.; Gregory, K. Carbon Emission and Mitigation Cost Comparisons between Fossil Fuel, Nuclear and Renewable Energy Resources for Electricity Generation. *Energy Policy* **2003**, *31* (13), 1315–1326.

(5)   Chen, M.; Paulson, S.; Thangadurai, V.; Birss, V. Sr-Rich Chromium Ferrites as Symmetrical Solid Oxide Fuel Cell Electrodes. *J. Power Sources* **2013**, *236*, 68–79.

(6)   Stambouli, A. B.; Traversa, E. Solid Oxide Fuel Cells (SOFCs): A Review of an Environmentally Clean and Efficient Source of Energy. *Renew. Sustain. Energy Rev.* **2002**, *6* (5), 433–455.

(7)   Ormerod, R. M. Solid Oxide Fuel Cells. *Chem. Soc. Rev.* **2003**, *32* (1), 17–28.

(8)   Dicks, A. L. Hydrogen Generation from Natural Gas for the Fuel Cell Systems of Tomorrow. *J. Power Sources* **1996**, *61* (1), 113–124.

(9)   Bloom Energy Server - Fuel Cell Energy Box | Bloom Energy http://www.bloomenergy.com/fuel-cell/energy-server/ (accessed Jan 17, 2017).

(10)   Ryan O'Hayre, Suk-Won Cha, Fritz B. Prinz, W. C. *Fuel Cell Fundamentals*; John Wiley & Sons, 2016.

(11)   Adler, S. B. Factors Governing Oxygen Reduction in Solid Oxide Fuel Cell Cathodes†. **2004**.

(12)   O'Hayre, R.; Barnett, D. M.; Prinz, F. B. The Triple Phase Boundary. *J.*

Electrochem. Soc. **2005**, *152* (2), A439.

(13) Chen, X. .; Khor, K. .; Chan, S. .; Yu, L. . Influence of Microstructure on the Ionic Conductivity of Yttria-Stabilized Zirconia Electrolyte. *Mater. Sci. Eng. A* **2002**, *335* (1), 246–252.

(14) Singhal, S. . Solid Oxide Fuel Cells for Stationary, Mobile, and Military Applications. *Solid State Ionics* **2002**, *152*, 405–410.

(15) Sammes, N. M.; Cai, Z. Ionic Conductivity of Ceria/yttria Stabilized Zirconia Electrolyte Materials. *Solid State Ionics* **1997**, *100* (1), 39–44.

(16) Bidrawn, F.; Kim, G.; Corre, G.; Irvine, J. T. S.; Vohs, J. M.; Gorte, R. J. Efficient Reduction of CO2 in a Solid Oxide Electrolyzer. *Electrochem. Solid-State Lett.* **2008**, *11* (9), B167–B170.

(17) Tsai, T.; Barnett, S. A. Effect of LSM-YSZ Cathode on Thin-Electrolyte Solid Oxide Fuel Cell Performance. *Solid State Ionics* **1997**, *93* (3), 207–217.

(18) Laguna-Bercero, M. A.; Kilner, J. A.; Skinner, S. J. Performance and Characterization of (La, Sr)MnO 3 /YSZ and La 0.6 Sr 0.4 Co 0.2 Fe 0.8 O 3 Electrodes for Solid Oxide Electrolysis Cells †. *Chem. Mater.* **2010**, *22* (3), 1134–1141.

(19) Tsoga, A.; Gupta, A.; Naoumidis, A.; Nikolopoulos, P. Gadolinia-Doped Ceria and Yttria Stabilized Zirconia Interfaces: Regarding Their Application for SOFC Technology. *Acta Mater.* **2000**, *48* (18), 4709–4714.

(20) Ebbesen, S. D.; Jensen, S. H. S. H.; Hauch, A.; Mogensen, M. B. High Temperature Electrolysis in Alkaline Cells, Solid Proton Conducting Cells, and Solid Oxide Cells. *Chem. Rev.* **2014**, *114* (21), 10697–10734.

(21) Park, S.; Vohs, J. M.; Gorte, R. J. Direct Oxidation of Hydrocarbons in a Solid-Oxide Fuel Cell. *Nature* **2000**, *404* (6775), 265–267.

(22) He, H.; Hill, J. M. Carbon Deposition on Ni/YSZ Composites Exposed to

Humidified Methane. *Appl. Catal. A Gen.* **2007**, *317* (2), 284–292.

(23) Zhang, Y.; Liu, B.; Tu, B.; Dong, Y.; Cheng, M. Redox Cycling of Ni-YSZ Anode Investigated by TPR Technique. *Solid State Ionics* **2005**, *176* (29–30), 2193–2199.

(24) Ishihara, T. *Perovskite Oxide for Solid Oxide Fuel Cells*; 2009.

(25) Boukamp, B. A. Fuel Cells: The Amazing Perovskite Anode. *Nat. Mater.* **2003**, *2* (5), 294–296.

(26) Fu, D.; Itoh, M. Ferroelectricity in Silver Perovskite Oxides. *Ferroelectr. - Mater. Asp.* **2011**, 413–442.

(27) Li, Z.; Yang, M.; Park, J. S.; Wei, S. H.; Berry, J. J.; Zhu, K. Stabilizing Perovskite Structures by Tuning Tolerance Factor: Formation of Formamidinium and Cesium Lead Iodide Solid-State Alloys. *Chem. Mater.* **2016**, *28* (1), 284–292.

(28) Setz, L. F. G.; Santacruz, I.; León-Reina, L.; De La Torre, A. G.; Aranda, M. A. G.; Mello-Castanho, S. R. H.; Moreno, R.; Colomer, M. T. Strontium and Cobalt Doped-Lanthanum Chromite: Characterisation of Synthesised Powders and Sintered Materials. *Ceram. Int.* **2015**, *41* (1), 1177–1187.

(29) Jiang, S. P.; Liu, L.; Ong, K. P.; Wu, P.; Li, J.; Pu, J. Electrical Conductivity and Performance of Doped LaCrO3 Perovskite Oxides for Solid Oxide Fuel Cells. *J. Power Sources* **2008**, *176* (1), 82–89.

(30) Oh, T. S.; Yu, A. S.; Adijanto, L.; Gorte, R. J.; Vohs, J. M. Infiltrated Lanthanum Strontium Chromite Anodes for Solid Oxide Fuel Cells: Structural and Catalytic Aspects. *J. Power Sources* **2014**, *262*, 207–212.

(31) Sfeir, J. LaCrO3-Based Anodes: Stability Considerations. *J. Power Sources* **2003**, *118* (1–2), 276–285.

(32) Jiang, S. P. A Review of Wet Impregnation - An Alternative Method for the Fabrication of High Performance and Nano-Structured Electrodes of Solid Oxide Fuel Cells. *Mater. Sci. Eng. A* **2006**, *418* (1–2), 199–210.

(33)   Ding, D.; Li, X.; Lai, S. Y.; Gerdes, K.; Liu, M. Enhancing SOFC Cathode Performance by Surface Modification through Infiltration. *Energy Environ. Sci.* **2014**, *7* (2), 552.

(34)   Tanaka, H.; Taniguchi, M.; Uenishi, M.; Kajita, N.; Tan, I.; Nishihata, Y.; Mizuki, J.; Narita, K.; Kimura, M.; Kaneko, K. Self-Regenerating Rh- and Pt-Based Perovskite Catalysts for Automotive-Emissions Control. *Angew. Chemie - Int. Ed.* **2006**, *45* (36), 5998–6002.

(35)   Nishihata, Y.; Mizuki, J.; Akao, T.; Tanaka, H.; Uenishi, M.; Kimura, M.; Okamoto, T.; Hamada, N. Self-Regeneration of a Pd-Perovskite Catalyst for Automotive Emissions Control. *Nature* **2002**, *418* (x), 164–167.

(36)   Adijanto, L.; Balaji Padmanabhan, V.; Küngas, R.; Gorte, R. J.; Vohs, J. M. Transition Metal-Doped Rare Earth Vanadates: A Regenerable Catalytic Material for SOFC Anodes. *J. Mater. Chem.* **2012**, *22* (22), 11396.

(37)   Busawon, A. N.; Sarantaridis, D.; Atkinson, A. Ni Infiltration as a Possible Solution to the Redox Problem of SOFC Anodes. **2008**, 186–189.

(38)   Neagu, D.; Oh, T. S.; Miller, D. N.; Menard, H.; Bukhari, S. M.; Gamble, S. R.; Gorte, R. J.; Vohs, J. M.; Irvine, J. T. Nano-Socketed Nickel Particles with Enhanced Coking Resistance Grown in Situ by Redox Exsolution. *Nat Commun* **2015**, *6*, 8120.

(39)   An, W.; Gatewood, D.; Dunlap, B.; Turner, C. H. Catalytic Activity of Bimetallic Nickel Alloys for Solid-Oxide Fuel Cell Anode Reactions from Density-Functional Theory. *J. Power Sources* **2011**, *196*, 4724–4728.

(40)   Takanabe, K.; Nagaoka, K.; Aika, K. I. Improved Resistance against Coke Deposition of Titania Supported Cobalt and Nickel Bimetallic Catalysts for Carbon Dioxide Reforming of Methane. *Catal. Letters* **2005**, *102* (3–4), 153–157.

(41)   Grgicak, C. M.; Pakulska, M. M.; O'Brien, J. S.; Giorgi, J. B.; O'Brien, J. S.;

Giorgi, J. B. Synergistic Effects of Ni1-xCox-YSZ and Ni1-xCux-YSZ Alloyed Cermet SOFC Anodes for Oxidation of Hydrogen and Methane Fuels Containing H2S. *J. Power Sources* **2008**, *183* (1), 26–33.

(42) Neagu, D.; Tsekouras, G.; Miller, D. N.; Menard, H.; Irvine, J. T. In Situ Growth of Nanoparticles through Control of Non-Stoichiometry. *Nat Chem* **2013**, *5* (11), 916–923.

(43) Xia, G.; Zhou, S.; Zhang, J.; Xu, J. Structural and Optical Properties of YAG:Ce3+ Phosphors by Sol-Gel Combustion Method. *J. Cryst. Growth* **2005**, *279* (3–4), 357–362.

(44) Chen, D.-H.; He, X.-R. Synthesis of Nickel Ferrite Nanoparticles by Sol-Gel Method. *Mater. Res. Bull.* **2001**, *36* (7–8), 1369–1377.

(45) High energy ball milling process for nanomaterial synthesis http://www.understandingnano.com/nanomaterial-synthesis-ball-milling.html.

(46) Diffraction, X.; Sources, I. Bragg ' S Law. *Production* **1970**, *5* (6), 371–372.

(47) McMullan, D. Scanning Electron Microscopy 1928–1965. *Scanning* **1995**, *17* (3), 175–185.

(48) CHROMacademy. Theory and Instrumentation of GC Sample Introduction. *Crawford Sci.* **2012**, 1–39.

(49) Orazem, M. E.; Tribollet, B. Electrochemical Impedance Spectroscopy. *Analysis* **2008**, 560.

(50) Chang, J. Y.; Kuan, Y. Der; Lee, S. M. Experimental Investigation of a Direct Methanol Fuel Cell with Hilbert Fractal Current Collectors. *J. Chem.* **2014**, *2014*.

(51) Sebastian, M. T. *Dielectric Materials for Wireless Communication*; 2008.

(52) Kovalevsky, A. V; Yaremchenko, A. A.; Populoh, S.; Weidenkaff, A.; Frade, J. R. Effect of A-Site Cation Deficiency on the Thermoelectric Performance of Donor-Substituted Strontium Titanate. *J. Phys. Chem. C* **2014**, *118* (9), 4596–4606.

(53) Janghorban, K.; Kirkaldy, J. S.; Weatherly, G. C. The Hume-Rothery Size Rule and Double-Well Microstructures in Gold-Nickel. *J. Phys. Condens. Matter* **2001**, *13* (38), 8661.

(54) Guillermet, F. Assessment of the Thermodynamic Properties of the Ni-Co System. *Zeitschrift für Met.* **1987**, *78* (9), 639–643.

(55) Jahangiri, A.; Aghabozorg, H.; Pahlavanzadeh, H. Effects of Fe Substitutions by Ni in La-Ni-O Perovskite-Type Oxides in Reforming of Methane with CO2 and O2. *Int. J. Hydrogen Energy* **2013**, *38* (25), 10407–10416.

(56) Rida, K.; Peña, M. a.; Sastre, E.; Martinez-Arias, A. Effect of Calcination Temperature on Structural Properties and Catalytic Activity in Oxidation Reactions of LaNiO3 Perovskite Prepared by Pechini Method. *J. Rare Earths* **2012**, *30* (3), 210–216.

(57) Konsolakis, M.; Sgourakis, M.; Carabineiro, S. A. C. Surface and Redox Properties of Cobalt–ceria Binary Oxides: On the Effect of Co Content and Pretreatment Conditions. *Appl. Surf. Sci.* **2015**, *341*, 48–54.

(58) Arriv??, C.; Delahaye, T.; Joubert, O.; Gauthier, G. Exsolution of Nickel Nanoparticles at the Surface of a Conducting Titanate as Potential Hydrogen Electrode Material for Solid Oxide Electrochemical Cells. *J. Power Sources* **2013**, *223*, 341–348.

(59) He, W.; Huang, H.; Chen, M.; Gao, J. F.; Chen, C. S. Stability and Oxygen Transport Property of La0.8Sr 0.2Cr0.5Fe0.5O3 -?? *Solid State Ionics* **2014**, *260*, 86–89.

(60) Zhang, Y.-Q.; Li, J.-H.; Sun, Y.-F.; Hua, B.; Luo, J.-L. Highly Active and Redox-Stable Ce-Doped LaSrCrFeO-Based Cathode Catalyst for CO 2 SOECs. *ACS Appl. Mater. Interfaces* **2016**, *8* (10), 6457–6463.

(61) Ding, X.; Liu, Y.; Gao, L.; Guo, L. Effects of Cation Substitution on Thermal

Expansion and Electrical Properties of Lanthanum Chromites. *J. Alloys Compd.* **2006**, *425* (1–2), 318–322.

(62) Ishihara, T.; Yan, J.; Shinagawa, M.; Matsumoto, H. Ni-Fe Bimetallic Anode as an Active Anode for Intermediate Temperature SOFC Using LaGaO3 Based Electrolyte Film. *Electrochim. Acta* **2006**, *52* (4), 1645–1650.

(63) Cooper, M.; Channa, K.; De Silva, R.; Bayless, D. J. Comparison of LSV/YSZ and LSV/GDC SOFC Anode Performance in Coal Syngas Containing H[sub 2]S. *J. Electrochem. Soc.* **2010**, *157* (11), B1713.

(64) Fabbri, E.; Pergolesi, D.; D'Epifanio, A.; Di Bartolomeo, E.; Balestrino, G.; Licoccia, S.; Traversa, E. Design and Fabrication of a Chemically-Stable Proton Conductor Bilayer Electrolyte for Intermediate Temperature Solid Oxide Fuel Cells (IT-SOFCs). *Energy Environ. Sci.* **2008**, *1* (3), 355.

(65) Zuo, C.; Zha, S.; Liu, M.; Hatano, M.; Uchiyama, M. Ba(Zr0.1Ce0.7Y0.2)O3-D as an Electrolyte for Low-Temperature Solid-Oxide Fuel Cells. *Adv. Mater.* **2006**, *18* (24), 3318–3320.

(66) Yao, W.; Duan, T.; Li, Y.; Yang, L.; Xie, K. Perovskite Chromate Doped with Titanium for Direct Carbon Dioxide Electrolysis. *New J. Chem.* **2015**, *39* (4), 2956–2965.

(67) Li, W.; Shi, Y.; Luo, Y.; Wang, Y.; Cai, N. Carbon Deposition on Patterned Nickel/yttria Stabilized Zirconia Electrodes for Solid Oxide Fuel Cell/solid Oxide Electrolysis Cell Modes. *J. Power Sources* **2015**, *276*, 26–31.

(68) Chen, T.; Wang, W. G.; Miao, H.; Li, T.; Xu, C. Evaluation of Carbon Deposition Behavior on the Nickel / Yttrium-Stabilized Zirconia Anode-Supported Fuel Cell Fueled with Simulated Syngas. *J. Power Sources* **2011**, *196* (5), 2461–2468.

(69) Nikolla, E.; Schwank, J.; Linic, S. Direct Electrochemical Oxidation of Hydrocarbon Fuels on SOFCs: Improved Carbon Tolerance of Ni Alloy Anodes. *J.*

Electrochem. Soc. **2009**, *156* (11), B1312.